Computer Methods in Applied Mechanics and Engineering 431 (2024) 117294

Contents lists available at ScienceDirect

Comput. Methods Appl. Mech. Engrg.

journal homepage: www.elsevier.com/locate/cma

A mortar segment-to-segment frictional contact approach in material point method

Weijian Liang [a], Huangcheng Fang [a], Zhen-Yu Yin [a,*], Jidong Zhao [b]

[a] Department of Civil and Environmental Engineering, The Hong Kong Polytechnic University, Hung Hom, Kowloon, Hong Kong
[b] Department of Civil and Environmental Engineering, Hong Kong University of Science and Technology, Clear Water Bay, Kowloon, Hong Kong

ARTICLE INFO

Keywords:
Material point method
Contact algorithm
Mortar method
Barrier method
Deformable grain

ABSTRACT

Handling contact problems in the Material Point Method (MPM) has long been a challenge. Traditional grid-based contact approaches often face issues with mesh dependency, while material point-based methods can be computationally intensive. To address these challenges, this study develops a novel mortar segment-to-segment frictional contact approach for MPM. We first introduce boundary vertices and propose an innovative kinematic update scheme for precise representation of the boundaries of the continuum media and their continuously evolving contact normals throughout the contact process. Then, we construct a weak form of contact constraints based on the mortar method to facilitate a stable segment-to-segment contact detection. To rigorously ensure the non-penetration condition, the energetic barrier method is further adopted and implemented in MPM for enforcing the contact constraints. The proposed kinematic update scheme for boundary vertices is first verified through a cantilever beam benchmark test. The verified framework is further examined through a wide range of contact scenarios, including rolling, sliding, collision of two rings, and multi-body contacts, in both small and finite deformations. The simulation results are thoroughly discussed, highlighting the significant improvements in accuracy and versatility. Potential limitations of the proposed method are also examined.

1. Introduction

Since its first introduction by Sulsky et al. [1,2] nearly three decades ago, MPM has evolved as a powerful and versatile computational tool for modeling complex engineering problems involving large deformations, where traditional finite element method (FEM) often struggles, like capturing the distinctive behavior of granular media [3–6], modeling snow anticrack formation and avalanche dynamics [7–10], complex solid-to-fluid transition of granular materials [11,12], fluid flow simulations [13–17], and the intricate hydro-mechanical coupling in porous media [18–25]. This success is largely attributed to the inherent flexibility of its innovative dual discretization: a Lagrangian description that represents the continuum using a set of material points tracked throughout the calculation, and a background grid employed to efficiently solve the continuum equations [26–28]. However, accurately modeling contact scenarios remains a prevalent challenge in MPM, limiting its applicability in various engineering problems where contact interactions play a crucial role.

Due to the single-value velocity field of the background mesh, MPM can naturally handle non-slip and impenetration interactions between different objects. However, this inherent feature can hardly account for free separation and frictional contact, thus falling short in comprehensively handling contact mechanics. The contact algorithm for MPM is pioneered by Bardenhagen et al. [29,30].

* Corresponding author.
E-mail address: zhenyu.yin@polyu.edu.hk (Z.-Y. Yin).

https://doi.org/10.1016/j.cma.2024.117294
Received 3 June 2024; Received in revised form 9 August 2024; Accepted 12 August 2024
Available online 20 August 2024

In this approach, the nodal velocity field of a specific body is compared with the combined nodal velocities from multiple bodies, and the nodes that exhibit influences from multiple bodies are identified as contact nodes. Owing to its straightforward and efficient nature, this grid-based contact strategy is followed by many [31–35] to gradually improve the performance of MPM contact. Nevertheless, these grid-based contact algorithms exhibit several noteworthy limitations. Firstly, they suffer from the issue of mesh dependency where contact is incorrectly detected due to shared influencing nodes, even when actual contact does not occur [36,37]. This issue is particularly prevalent in MPM variants with larger support domains, *e.g.*, B-spline MPM [38,39], CPDI [40,41]. Additionally, these methods often rely on mass or volume gradients to estimate the contact normal, which can lead to inaccuracies due to evolving particle positions and their distribution. Furthermore, accurately resolving contact in quasi-static cases is highly challenging, as the velocity variation is negligible [36,37,42].

In recent years, there has been a growing trend of using material points themselves or alternative representations to determine the contact surface. For instance, Nairn et al. [37] employs a statistical model, logistic regression (LR), to distinguish point clouds of contacting bodies and construct contact normal vectors. Although accurately retrieving contact pressures and areas remains challenging in scenarios involving small deformations between stiff objects, this approach largely mitigates the aforementioned limitations of grid-based contact methods. Chen et al. [36] and de Vaucorbeil and Nguyen [43], following the principles of the Discrete Element Method (DEM), directly utilize material points from contacting bodies to establish point-to-point contacts and evaluate the contact response. This approach offers an effective and intuitive pathway. However, it also inherits the computationally intensive nature of DEM, with the contact cost potentially scaling as $\mathcal{O}(n^2)$, where n denotes the number of material points. Alternatively, Liu and Sun [44] introduces a level-set approach to identify an unbiased contact surface and generate the contact gap function. Guilkey et al. [42] defines the contact domain continuum using boundary material points and employs a penalty method for contact forces. Coupling MPM with methods like DEM also presents an alternative for modeling multi-body interactions, particularly in scenarios involving both soft and rigid bodies [45,46]. However, our focus remains on MPM-specific contact algorithms, and these hybrid approaches are out the scope of the current study.

In this study, we propose an innovative mortar segment-to-segment frictional contact approach for MPM to accurately model a broad range of contact problems in either small to finite deformations, including rolling, sliding, collision and multi-body contacts. Drawing inspiration from the prior work of Guilkey et al. [42], we introduce a set of boundary vertices and corresponding line segments to precisely represent the boundaries of the contact domain and their contact normals. To account for the dynamically evolving contact geometry, we propose the weighting function augmentation and a new kinematic update scheme tailored for these boundary vertices to improve their interpolation with the background mesh. With the boundary segments, we employ the mortar method, which has demonstrated substantial efficacy in other continuum methods [47–51], to construct segment-to-segment contact detection between bodies in potential contact, bypassing the reliance on grid-based velocity fields. This treatment converts the strong, pointwise contact constraints to a weak form across contact interfaces, offering more stable and robust predictions for the contact response. Finally, we deploy an energetic barrier method to rigorously enforce the non-penetration constraint without introducing penalty parameters. In fact, the barrier method is gaining popularity as an approach for coupling MPM with other methods, such as MPM-FEM [46], MPM-DEM [52], coupled MPM and level set methods [53], as well as in soil–structure interactions modeling [54].

The paper is organized as follows: Section 2 describes the formulations of MPM. Section 3 presents rigorous details of the proposed contact algorithm, including the introduction of boundary vertices, mortar method-based discretization, contact enforcement via the barrier method, as well as the complete computational procedure, while Section 4 demonstrate the capabilities of the proposed contact algorithm through several examples. The paper concludes in Section 5. Throughout this work, the following notation is adopted: subscript p, I and v denote the variables associated with material point, grid node and boundary vertex respectively; $\dot{\square}$ and $\ddot{\square}$ represent first and second-order material time derivatives; $\otimes$ indicates the dyadic product; $\cdot$ and $:$ denote single and double contraction of tensor indices, respectively.

2. Formulation of MPM

2.1. Governing equations

As illustrated in Fig. 1, we consider two deformable bodies denoted as the slave body $\mathcal{B}_s$ and the master body $\mathcal{B}_m$, undergoing large deformations and contact interaction. Their current configurations are represented by $\mathcal{B}_s^t$ and $\mathcal{B}_m^t$, respectively. The boundaries of each body include the contact surfaces Γ_c^s for the slave and Γ_c^m for the master, along with the Dirichlet boundary Γ_d, and the Neumann boundary Γ_t. The kinematics and deformation of each continuum body in its current configuration are governed by the conservation of momentum, expressed as follows:

$$\frac{\mathrm{D}\rho}{\mathrm{D}t} = 0, \tag{1}$$

$$\rho \boldsymbol{a} = \nabla \cdot \boldsymbol{\sigma} + \rho \boldsymbol{g}, \tag{2}$$

where ρ is the density, $\boldsymbol{a}$ denotes the acceleration, $\boldsymbol{\sigma}$ is the Cauchy stress tensor, and $\boldsymbol{g}$ is the gravitational acceleration. In MPM, the continuum domain is discretized into a number of Lagrangian material points which carry mass, momentum, and other internal variables, *e.g.*, deformation gradient $\boldsymbol{F}$. Since these material points retain their mass throughout the computation, the conservation of mass is automatically satisfied.

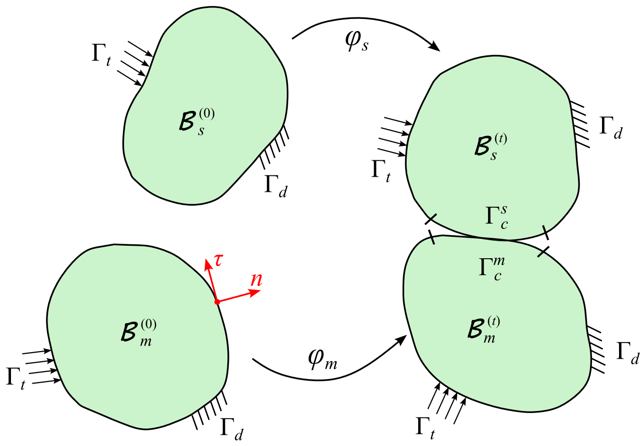

Fig. 1. Illustration of contact analysis in large deformation.

Following the standard weighted residual procedure, the momentum conservation can be written in below the variational form:

$$\int_{\Omega} \rho \boldsymbol{a} \cdot \delta \boldsymbol{v} \, d\Omega + \int_{\Omega} \boldsymbol{\sigma} : \nabla \delta \boldsymbol{v} \, d\Omega = \int_{\Omega} \rho \boldsymbol{g} \cdot \delta \boldsymbol{v} \, d\Omega + \int_{\Gamma_c} \boldsymbol{t}^c \cdot \delta \boldsymbol{v} \, dS + \int_{\Gamma_t} \boldsymbol{t} \cdot \delta \boldsymbol{v} \, dS, \tag{3}$$

where $\delta \boldsymbol{v}$ is an admissible velocity field variation, $\boldsymbol{t}^c$ and $\boldsymbol{t}$ denotes the contact traction and the ordinary boundary traction, respectively. Herein, we distinguish the contact traction from the other forms of boundary traction for better clarity.

2.2. Particle to grid interpolation

In this study, the updated Lagrangian formulation is adopted. At the beginning of each step, the mass and momentum of each particle are mapped to the background grid to obtain the nodal velocity. In the current work, the APIC scheme proposed by Jiang et al. [55,56] is adopted. This scheme considers the affine velocity field of material points and also transfers them onto the background mesh, realizing more stable simulations and overcoming the dissipation of angular momentum in PIC:

$$m_I = \sum_{p=1}^{n_p} S_{Ip} m_p, \tag{4}$$

$$\boldsymbol{p}_I^t = \sum_{p=1}^{n_p} S_{Ip} m_p \left(\boldsymbol{v}_p^t + \boldsymbol{B}_p^t \cdot (\boldsymbol{D}_p^t)^{-1} \cdot (\boldsymbol{x}_I - \boldsymbol{x}_p^t) \right), \tag{5}$$

$$\boldsymbol{v}_I^t = \frac{\boldsymbol{p}_I^t}{m_I}, \tag{6}$$

where m_I, $\boldsymbol{p}_I^t$, and $\boldsymbol{v}_I^t$ represent the mass, momentum, and velocity of node I, respectively, n_p is the number of material points, $S_{Ip} := S_I(\boldsymbol{x}_p^t)$ is the nodal weighting function evaluated at $\boldsymbol{x}_p^t$ [57], and $\boldsymbol{B}_p^t$ and $\boldsymbol{D}_p^t$ are two additional material point properties related to the surrounding velocity field that are defined as follows:

$$\boldsymbol{B}_p = \sum_{p=1}^{n_p} S_{Ip} \boldsymbol{v}_p \otimes \left(\boldsymbol{x}_I - \boldsymbol{x}_p \right), \tag{7}$$

$$\boldsymbol{D}_p = \sum_{p=1}^{n_p} S_{Ip} \left(\boldsymbol{x}_I - \boldsymbol{x}_p \right) \otimes \left(\boldsymbol{x}_I - \boldsymbol{x}_p \right). \tag{8}$$

These two matrices are update at the end of each step as shown later in Eq. (25) and (26). It is noted that Nakamura et al. [58] recently presents a variant of the APIC scheme named Taylor-PIC (TPIC), which combines affine velocity fields based on the first-order Taylor series approximation with traditional PIC transfer, *i.e.*,

$$\boldsymbol{p}_I = \sum_{p=1}^{n_p} S_{Ip} m_p \left(\boldsymbol{v}_p + \nabla \boldsymbol{v}_p \cdot (\boldsymbol{x}_I - \boldsymbol{x}_p) \right). \tag{9}$$

It is expected that this alternative method can yield similar result as APIC and is not explored in this work.

2.3. Deformation and stress update

Using the nodal velocity, the velocity gradient $\boldsymbol{L}$ and deformation gradient $\boldsymbol{F}$ for each material point can be updated as follows:

$$\boldsymbol{L}_p^t = \sum_{I=1}^{n_n} \nabla S_{Ip} \boldsymbol{v}_I^t, \tag{10}$$

$$\boldsymbol{F}_p^t = (\Delta t \boldsymbol{L}_p^t + \boldsymbol{I}) \boldsymbol{F}_p^{t-1}, \tag{11}$$

where $\boldsymbol{I}$ is the identity matrix and $\nabla S_{Ip} := \nabla S_I(\boldsymbol{x}_p^t)$ denotes the gradient of the weighting function.

Employing linear elastic models, the Cauchy stress for each particle can be computed incrementally as follows:

$$\Delta \boldsymbol{\varepsilon}_p^t = \frac{1}{2} \Delta t \left(\boldsymbol{L}_p^t + \boldsymbol{L}_p^{t\,T} \right), \tag{12}$$

$$\boldsymbol{\sigma}_p^t = \boldsymbol{\sigma}_p^{t-1} + \mathbb{D} : \Delta \boldsymbol{\varepsilon}_p^t, \tag{13}$$

where $\mathbb{D}$ is the elastic tensor. In the case of finite deformations with significant rigid rotations, an appropriate objective stress rate should be used. By employing the Jaumann stress rate [59], *i.e.*, $\boldsymbol{\sigma}^{\nabla J} = \dot{\boldsymbol{\sigma}} + \boldsymbol{\sigma} \cdot \boldsymbol{W} - \boldsymbol{W} \cdot \boldsymbol{\sigma}$, the Cauchy stress can then be computed by integrating over time as follows:

$$\boldsymbol{\sigma}_p^t = \boldsymbol{\sigma}_p^{t-1} + \mathbb{D} : \Delta \boldsymbol{\varepsilon}_p^t + \Delta t (\boldsymbol{W}_p^t \cdot \boldsymbol{\sigma}_p^{t-1} - \boldsymbol{\sigma}_p^{t-1} \cdot \boldsymbol{W}_p^t), \tag{14}$$

where $\boldsymbol{W}_p^t$ is the skew part of the velocity gradient, commonly denoted the spin tensor, and is computed as below:

$$\boldsymbol{W}_p^t = \frac{1}{2} \left(\boldsymbol{L}_p^t - \boldsymbol{L}_p^{t\,T} \right). \tag{15}$$

Regarding the material point domain, various update schemes are available, including static domain (uGIMP), deformation proportional to $\det(\boldsymbol{F})$ [57], updates based on principal components of the deformation gradient F_{ii} [40], and updates using principal components of the stretch tensor U_{ii} [60]. Given that static domains (uGIMP) can hardly handle volume changes, and updating with F_{ii} can cause domains to diminish under large rotations (see [40]), we resort to the diagonal components of the stretch tensor U_{ii} for particle domain updates. This approach is particularly suitable for cases involving potential large deformations, rotations, and complex interactions among deformable bodies during contact interaction.

$$l_i^t = U_{ii}^t l_i^0, \quad (i = x, y \quad \text{and no implied sum on } i) \tag{16}$$

where l_i denotes the material point extend along the i-direction, U_{ii} represents the diagonal components of the stretch tensor which associated with the deformation gradient via $\boldsymbol{U} = \left(\boldsymbol{F}^T \boldsymbol{F} \right)^{\frac{1}{2}}$ [4].

2.4. Grid update

After discretization, the weak form of the momentum equation (Eq. (3)) can be expressed on the background mesh as follows:

$$\dot{\boldsymbol{p}}_I = \boldsymbol{f}_I^{\text{int}} + \boldsymbol{f}_I^{\text{ext}} + \boldsymbol{f}_I^{\text{con}} + \boldsymbol{f}_I^{\text{damp}} \tag{17}$$

with

$$\boldsymbol{f}_I^{\text{int}} = - \sum_{p=1}^{n_p} \boldsymbol{\sigma}_p : \nabla S_{Ip} V_p, \tag{18}$$

$$\boldsymbol{f}_I^{\text{ext}} = \sum_{p=1}^{n_p} m_p \boldsymbol{b} S_{Ip} + \int_{\partial\Omega} N_I \boldsymbol{t} \, dS, \tag{19}$$

$$\boldsymbol{f}_I^{\text{damp}} = -\alpha_{\text{damp}} m_I \sqrt{\frac{E}{\rho h^2}} \boldsymbol{v}_I^t. \tag{20}$$

Here, $\boldsymbol{f}_I^{\text{int}}$ and $\boldsymbol{f}_I^{\text{ext}}$ are the internal and external nodal forces, respectively, and $\boldsymbol{f}_I^{\text{con}}$ denotes the contact force, which will be detailed in Section 3. Additionally, a damping force [50] is considered to reduce stress fluctuations in modeling quasi-static problems. Here, α_{damp} is a non-dimensional damping coefficient, h is the element width of the background mesh, and E and ρ are the Young's modulus and density of the material being modeled, respectively. Note that, multi-layer background mesh is adopted in current study which permits interpenetration between two colliding objects if $\boldsymbol{f}_I^{\text{con}}$ is not evaluated.

2.5. Kinematic update

Upon obtaining the nodal solution for the momentum equation (Eq. (17)), the updated nodal information is transferred back to the material points for facilitating the update of their respective positions and velocities. The particle velocity is updated as follows:

$$\boldsymbol{v}_p^{t+1} = \alpha_{\text{pic}} \boldsymbol{v}_{\text{pic}}^{t+1} + (1 - \alpha_{\text{pic}}) \boldsymbol{v}_{\text{flip}}^{t+1}, \tag{21}$$

with

$$\boldsymbol{v}_{\text{pic}}^{t+1} = \sum_{I=1}^{n_n} \boldsymbol{v}_I^{t+1} S_{Ip}, \tag{22}$$

$$\boldsymbol{v}_{\text{flip}}^{t+1} = \boldsymbol{v}_p^t + \Delta t \sum_{I=1}^{n_n} \boldsymbol{a}_I^{t+1} S_{Ip}, \tag{23}$$

where n_n is the number of nodes, $\boldsymbol{v}_I^{t+1}$ represents the updated velocity at node I. The terms $\boldsymbol{v}_{\text{pic}}$ and $\boldsymbol{v}_{\text{flip}}$ represent the updated particle velocities based on the PIC [61] and FLIP [62] schemes, respectively, and α_{pic} denotes the proportionate contribution of the PIC velocity within this linear combination. The PIC scheme directly employs nodal velocities to overwrite the existing particle velocities, providing better numerical stability but with excessive energy dissipation [63]. In contrast, the FLIP method incrementally updates the material point velocities using nodal accelerations, mitigating the issue of energy dissipation at the expense of introducing computational noise and potentially reducing stability [63]. The combination of these two approaches aims to inherit their respective advantages.

The material point position, $\boldsymbol{x}_p$, is updated based on the convection of the background mesh:

$$\boldsymbol{x}_p^{n+1} = \boldsymbol{x}_p^n + \Delta t \sum_{I=1}^{n_n} \boldsymbol{v}_I^{t+1} S_{Ip}. \tag{24}$$

Lastly, the affine matrices $\boldsymbol{B}_p^{t+1}$ and $\boldsymbol{D}_p^{t+1}$ used in APIC scheme are updated as follows [55,56,64]:

$$\boldsymbol{B}_p^{t+1} = \sum_{p=1}^{n_n} S_{Ip} \boldsymbol{v}_p^{t+1} \otimes \left(\boldsymbol{x}_I - \boldsymbol{x}_p^t\right), \tag{25}$$

$$\boldsymbol{D}_p^{t+1} = \sum_{p=1}^{n_n} S_{Ip} \left(\boldsymbol{x}_I - \boldsymbol{x}_p^t\right) \otimes \left(\boldsymbol{x}_I - \boldsymbol{x}_p^t\right). \tag{26}$$

3. Contact algorithm

3.1. Boundary vertex

One pivotal prerequisite for effectively resolving the contact interaction is the precise identification of the boundary for each body potentially in contact. Previous grid-based contact algorithms rely on the background grid, where the momentum equation is solved, for contact detection, exhibiting a dependency on the mesh resolution. To address this, we introduce boundary vertices to represent the surface of the continuous body with desired accuracy, as shown in Fig. 2. Unlike internal material points, these boundary vertices do not carry state variables such as volume, mass, stress, or strain. Instead, they are designed to move with the continuum body in a conforming manner and serve to delineate the boundary of the domain solely. This treatment not only facilitates precise contact detection and determination of the contact normal vector but also aids in enforcing contact forces and other generic types of Neumann boundary conditions shown in Fig. 1.

3.1.1. Augmented weighting function

Due to the dual representation (*i.e.*, particles and background mesh) in MPM, the boundary vertices still rely on the weighting function to interact with the background mesh, including imposing contact constraints and updating their own kinematics. Similar to ordinary material points, we define the *unmodified* weighting function for a boundary vertex as $S_{Iv} := S_I(\boldsymbol{x}_v)$, where $\boldsymbol{x}_v$ is the coordinate of a boundary vertex. As shown in Fig. 2, the support of the weighting functions for the boundary vertices can extend beyond the physical domain of the body and be larger than those of all material points. This mismatch results in several fringe nodes, which only interact with the boundary vertices but are null in any physical field like mass and momentum. Consequently, involving those fringe nodes in the mapping would inevitably lead to erroneous or unstable computations.

To address this issue, we propose an augmented weighting function for the data transfer between the boundary vertex and the mesh, expressed as:

$$\bar{S}_{Iv} = \frac{S_{Iv} m_I}{\sum_I^{n_I} S_{Iv} m_I}. \tag{27}$$

Here, $\bar{S}_{Iv}$ represents the augmented weighting function, and m_I is the nodal mass. This augmentation strategically uses the nodal mass to truncate its support, effectively preventing it from extending beyond the physical domain, while simultaneously maintaining compliance with the partition of unity requirement. Although the velocity modification reported by Guilkey et al. [42] could achieve a similar purpose, our proposed method offers a more foundational improvement, as the augmented weighting functions can also be utilized for other purposes, such as distributing concentrated forces from the vertex to associated nodes.

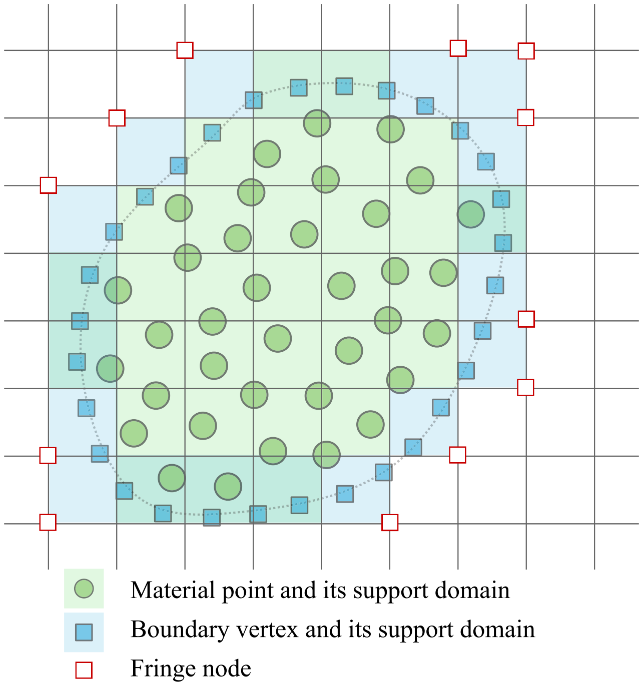

Fig. 2. Schematic of boundary vertices and their supporting domain in standard MPM.

3.1.2. Affine kinematic update

Since these boundary nodes do not carry mass, they cannot directly apply the APIC update scheme [55,56] as the internal material points do (see Eq. (5)). This limitation could lead to an increasing discrepancy in their configuration against the continuum domain, especially in the presence of large rotations, as demonstrated in Section 4.1. To address this discrepancy and ensure that the boundary vertices move in alignment with internal material points, we propose a new affine-type kinematic update scheme for the boundary vertices.

Firstly, we approximate the angular velocity field for a node via a weighted average of the angular velocities of neighboring material points:

$$\boldsymbol{\omega}_I^t = \frac{1}{m_I} \sum_p^{n_p} S_{Ip} \boldsymbol{\omega}_p^t m_p, \tag{28}$$

where $\boldsymbol{\omega}_p^t$ is the angular velocity of material point p, obtained from the spin tensor (Eq. (15)), and $\boldsymbol{\omega}_I^t$ represents the effective angular velocity at node I, calculated as a weighted average. While a more mathematically rigorous approach could involve using the moment of inertia, the current choice provides a sufficiently accurate result and does not require determining an additional nodal quantity.

Upon obtaining the nodal angular velocity field, the velocity of a boundary vertex $\boldsymbol{v}_v^{t+1}$ is then determined based on $\boldsymbol{v}_I$ and $\boldsymbol{\omega}_I^t$, taking into account the surrounding affine velocity field and following the core idea of APIC transfer:

$$\boldsymbol{v}_v^{t+1} = \sum_I^{n_I} \bar{S}_{Iv} \left(\boldsymbol{v}_I^t + \boldsymbol{\omega}_I^t \times (\boldsymbol{x}_v^t - \boldsymbol{x}_I) \right), \tag{29}$$

$$\boldsymbol{x}_v^{t+1} = \boldsymbol{x}_v^t + \boldsymbol{v}_v^{t+1} \Delta t. \tag{30}$$

As will be demonstrated later, this new update scheme, together with the weighting function augmentation, effectively handle the motion of boundary vertices, ensuring their alignment with the overall deformation of the material body, even in simulations involving large rotations, and laying a solid foundation for the subsequent contact detection and enforcement.

3.2. Contact constraint

We define a gap function $g(\boldsymbol{x}_s, t)$ on the slave surface (note that the master and slave surfaces can be defined interchangeably) as the fundamental measure of the distance between the slave and master bodies in their current configuration (Fig. 3(a)). The gap function is defined as follows:

$$g(\boldsymbol{x}_s, t) = -\boldsymbol{n}(\boldsymbol{x}_s) \cdot (\boldsymbol{x}_s - \bar{\boldsymbol{x}}_m), \tag{31}$$

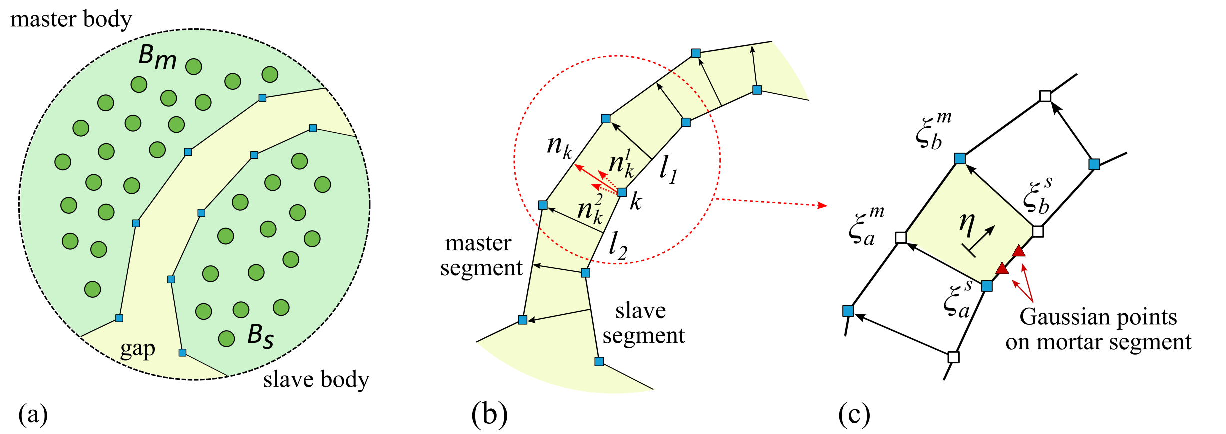

Fig. 3. Schematic of segment-to-segment contact in MPM: (a) contact detection between master body and slave body, (b) unit normal vector $\boldsymbol{n}$ on the slave surface (c) numerical integration for each mortar segment.

where $\boldsymbol{n}$ is the outward unit normal vector at $\boldsymbol{x}_s$ on the slave surface, and $\bar{\boldsymbol{x}}_m$ denotes the projection of $\boldsymbol{x}_s$ onto the master surface along $\boldsymbol{n}$. The negative sign is added to ensure that the gap function is positive when non-penetration condition is hold.

The contact between two deformable bodies follows the classical Karush–Kuhn–Tucker (KKT) conditions, which can be stated as:

$$g(\boldsymbol{x}_s, t) \geq 0, \qquad \text{Impenetrability} \tag{32}$$

$$t_n^c(\boldsymbol{x}_s, t) \leq 0, \qquad \text{Non-tension} \tag{33}$$

$$g \cdot t_n^c = 0, \qquad \text{Complementarity} \tag{34}$$

where t_n^c is the normal component of contact pressure $\boldsymbol{t}^c$, which must be non-positive (indicating compression) when contact occurs.

To enforce the contact constraint, we introduce a Lagrange multiplier and use it to represent the *negative* of the contact traction:

$$\boldsymbol{\lambda} = \lambda^n \boldsymbol{n} + \lambda^\tau \boldsymbol{\tau} = -\boldsymbol{t}^c, \tag{35}$$

where $\boldsymbol{\tau}$ is the unit shear vector as shown in Fig. 1.

Substituting the Lagrange multiplier into Eq. (32) and integrating over the slave surface, we obtain the weak form of the impenetration condition as follows:

$$\int_{\Gamma_c^s} \delta\lambda^n g(\boldsymbol{x}_s, t)\mathrm{d}\Gamma \geq 0, \qquad \forall \delta\lambda^n \in \delta\Lambda \tag{36}$$

where $\delta\Lambda$ denotes the test space for the variation $\delta\lambda^n$.

3.3. Spatial discretization

Following the standard FEM discretization, the gap can be interpolated by the displacement on the slave and master surfaces, which can be expressed as:

$$g(\boldsymbol{x}_s) = \boldsymbol{n}_s(\boldsymbol{x}_s) \cdot \left[\sum_{i=1}^{n_v^s} N_i(\boldsymbol{x}_s)\boldsymbol{x}_i - \sum_{j=1}^{n_v^m} N_j(\bar{\boldsymbol{x}}_m)\boldsymbol{x}_j \right], \tag{37}$$

where n_v^s and n_v^m are the numbers of boundary vertices on the slave and master surfaces, respectively, $\boldsymbol{x}_\square$ represents the coordinate of boundary vertex and $N_\square$ is the standard linear shape function.

Likewise, the Lagrange multiplier defined on the slave surface can be discretized in terms of the nodal values. As reported in [49,65], different basis functions can be chosen for the Lagrange multiplier to form dual Lagrange interpolation, which could improve the condition of the system matrix. Since the current study focuses on explicit MPM without intensive matrix operations, adopting standard FEM shape functions that are identical to those used in the displacement interpolation is considered sufficient:

$$\lambda(\boldsymbol{x}_s) = \sum_{k=1}^{n_v^s} N_k(\boldsymbol{x}_s)\lambda_k, \tag{38}$$

By substituting the displacement and Lagrange multiplier expressions into the weak form of the non-penetration condition outlined in Eq. (36) and interchanging the integral and summation, we obtain the discretized condition, which is expressed as follows:

$$\begin{aligned}
&\int_{\Gamma_c^s} g(\boldsymbol{x}_s, t)\delta\lambda^n \mathrm{d}\Gamma \geq 0 \\
&= \int_{\Gamma_c^s} \boldsymbol{n}_s(\boldsymbol{x}_s)\cdot\left[\sum_{i=1}^{n_v^s} N_i(\boldsymbol{x}_s)\boldsymbol{x}_i - \sum_{j=1}^{n_v^m} N_j(\bar{\boldsymbol{x}}_m)\boldsymbol{x}_j\right]\sum_{k=1}^{n_v^s} N_k(\boldsymbol{x}_s)\delta\lambda_k^n \mathrm{d}\Gamma \\
&= \sum_{k=1}^{n_v^s} \boldsymbol{n}_s(\boldsymbol{x}_s)\cdot\left[\sum_{i=1}^{n_v^s}\int_{\Gamma_c^s} N_k(\boldsymbol{x}_s)N_i(\boldsymbol{x}_s)\boldsymbol{x}_i \mathrm{d}\Gamma - \sum_{j=1}^{n_v^m}\int_{\Gamma_c^s} N_k(\boldsymbol{x}_s)N_j(\bar{\boldsymbol{x}}_m)\boldsymbol{x}_j \mathrm{d}\Gamma\right]\delta\lambda_k^n \geq 0
\end{aligned} \tag{39}$$

Considering the arbitrariness of $\delta\lambda_k^n$ at all boundary vertices $k \in [1, 2, \dots, n_v^s]$, the above equation can be reformulated as a discrete gap for a single boundary vertex $\boldsymbol{x}_k$ as:

$$\begin{aligned}
\widetilde{g}_k &= \boldsymbol{n}_k \cdot \left[\sum_{i=1}^{n_v^s}\int_{\Gamma_c^s} N_k(\boldsymbol{x}_s)N_i(\boldsymbol{x}_s)\boldsymbol{x}_i \mathrm{d}\Gamma - \sum_{j=1}^{n_v^m}\int_{\Gamma_c^s} N_k(\boldsymbol{x}_s)N_j(\bar{\boldsymbol{x}}_m)\boldsymbol{x}_j \mathrm{d}\Gamma\right] \\
&= \boldsymbol{n}_k \cdot \left[\sum_{i=1}^{n_v^s} D_{ki}\boldsymbol{x}_i - \sum_{j=1}^{n_v^m} M_{kj}\boldsymbol{x}_j\right] \geq 0, \qquad k \in [1, 2, \dots, n_v^s]
\end{aligned} \tag{40}$$

Here, the continuous normal vector $\boldsymbol{n}_s(\boldsymbol{x}_s)$ is replaced with a discrete vertex value $\boldsymbol{n}_k$. As shown in Fig. 3(c), $\boldsymbol{n}_k$ can be evaluated as:

$$\boldsymbol{n}_k = \frac{\boldsymbol{n}_k^1 l_1 + \boldsymbol{n}_k^2 l_2}{\|\boldsymbol{n}_k^1 l_1 + \boldsymbol{n}_k^2 l_2\|}, \tag{41}$$

where $\boldsymbol{n}_k^{\square}$ and $l_{\square}$ are, respectively, the outward normal vector and the length of line segment connected to boundary vertex k as shown in Fig. 3(c). While D_{ki} and M_{kj} are components of the mortar matrices $\boldsymbol{\mathcal{D}} \in \mathbb{R}^{n_v^s \times n_v^s}$ and $\boldsymbol{\mathcal{M}} \in \mathbb{R}^{n_v^s \times n_v^m}$, respectively, which are defined as:

$$D_{ki} = \int_{\Gamma_c^s} N_k(\boldsymbol{x}_s)N_i(\boldsymbol{x}_s)\mathrm{d}\Gamma, \qquad \text{for} \quad k, i \in [1, 2, \dots, n_v^s] \tag{42}$$

$$M_{kj} = \int_{\Gamma_c^s} N_k(\boldsymbol{x}_s)N_j(\bar{\boldsymbol{x}}_m)\mathrm{d}\Gamma, \qquad \text{for} \quad k \in [1, 2, \dots, n_v^s], \quad j \in [1, 2, \dots, n_v^m] \tag{43}$$

In numerical implementation, the integration domain Γ_c^s will be decomposed into simpler, manageable parts named mortar segments, based on the slave vertices and the projected master vertices as depicted in Fig. 3(c). The integral is subsequently evaluated using the Gauss–Legendre quadrature over all mortar segments, which is expressed as:

$$D_{ki} = \sum_{l=1}^{n_{seg}}\left(\sum_{g=1}^{n_{gp}} w_g N_k(\xi^s(\eta_g))N_i(\xi^s(\eta_g))J_l\right), \tag{44}$$

$$M_{kj} = \sum_{l=1}^{n_{seg}}\left(\sum_{g=1}^{n_{gp}} w_g N_k(\xi^s(\eta_g))N_j(\xi^m(\bar{\eta}_g))J_l\right) \tag{45}$$

Here, $\eta \in [0, 1]$ defines the parametrization of a mortar segment, ξ_a^s and ξ_b^s, as well as ξ_a^m and ξ_b^m denote the local element coordinates of the endpoints of the mortar segment on the slave and master surfaces, respectively, as shown in Fig. 3(c). n_{seg} represents the number of decomposed mortar segments, n_{gp} is the number of Gaussian points used within each mortar segment, which is set to 2 in the current study. J_l denotes the Jacobian of the l-th mortar segment. The numerical evaluation of the mortar matrices $\boldsymbol{\mathcal{D}}$ and $\boldsymbol{\mathcal{M}}$ is demonstrated in Algorithm 1. For additional information on the numerical evaluation of the mortar matrix, readers can refer to [66].

To ensure that the weighted gap distance $\bar{g}_k$ has the correct unit, we could perform regularization by normalizing $\widetilde{g}_k$ with the weighted segment length (2D) or area (3D) on boundary vertex k which is computed by the summation over the corresponding row of the mortar matrix $\boldsymbol{\mathcal{D}}$:

$$\bar{g}_k = \widetilde{g}_k / \sum_{i=1}^{n_v^s} D_{ki} \tag{46}$$

Algorithm 1 Numerical evaluation of mortar matrices

1: Construct the unit normal vectors $\boldsymbol{n}$ on the slave surface.
2: Project all master vertices onto the slave surface along $\boldsymbol{n}$ to obtain the projected master vertices $\bar{\boldsymbol{x}}_s$.
3: Construct mortar segment based on the projected master vertices $\bar{\boldsymbol{x}}_s$ and slave vertices $\boldsymbol{x}_s$, and evaluate the Jacobian determinant for each mortar segment.
4: Determine Gaussian points with coordinate η_g, and obtain $\xi^s(\eta_g)$ and $N(\xi^s(\eta_g))$ with respect to the slave vertices. Project gaussian points onto master surface to obtain $\bar{\eta}_g$, and compute $\xi^m(\bar{\eta}_g)$ and $N(\xi^m(\bar{\eta}_g))$ with respect to the master vertices.
5: Compute D_{ki} and M_{kj} of the mortar matrices $\boldsymbol{D}$ and $\boldsymbol{\mathcal{M}}$.

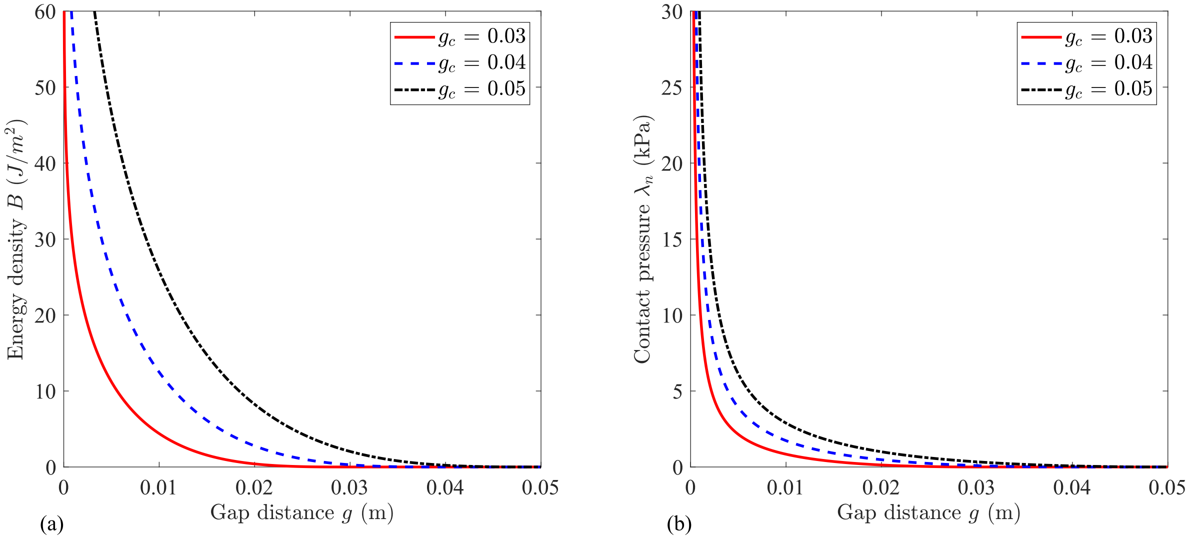

Fig. 4. The relationship between barrier energy and contact pressure with respect to gap distance.

3.4. Contact enforcement

3.4.1. Normal contact enforcement via barrier method

Up to now, we have transformed the continuum contact constraint into a weak form constraint for boundary vertices using the mortar segment-to-segment approach. To enforce these contact constraints, various methods can be utilized. One common approach is the penalty method, which permits interpenetration to some extent and derives the contact force by multiplying the contact overlap with a penalty factor [42]. Alternatively, we resort to the energetic barrier method for contact enforcement. Compared to the penalty method, the barrier method allows for a very small gap between two contacting surfaces, acknowledging that a small gap realistically exists in the real world due to microscopic asperities [67]. The energy associated with this gap is defined by a barrier energy function $B(g)$ [67,68], which reads as:

$$B(g) := \begin{cases} -\kappa(g - g_c)^2 \ln\left(\dfrac{g}{g_c}\right), & \text{for } 0 < g \le g_c, \\ 0, & \text{otherwise,} \end{cases} \tag{47}$$

where g_c denotes the critical gap which controls the threshold for establishing a contact pair, g is the gap between the master and slave surfaces, and is selected as the weighted gap $\bar{g}$ (Eq. (46)) in this study. Additionally, κ indicates the stiffness of the barrier (contact) and has the unit of pressure per length.

By taking the derivative of barrier energy with respect to the gap distance, the normal contact pressure can be obtained as follows:

$$\lambda^n := -\frac{\partial B(g)}{\partial g} = \begin{cases} \kappa(g - g_c)\left[2\ln\left(\dfrac{g}{g_c}\right) - \dfrac{g_c}{g} + 1\right], & \text{for } 0 \le g \le g_c, \\ 0, & \text{otherwise.} \end{cases} \tag{48}$$

Fig. 4 presents the relationship between barrier energy and contact pressure against the gap distance. As observed from Eqs. (47), (48), and Fig. 4, it is evident that as the gap g approaches zero, both the potential energy and the contact pressure increase towards infinity ($B(g) \to +\infty$, $\lambda^n \to +\infty$). This behavior effectively prevents the gap from further reduction, thereby fulfilling the non-penetration constraint prescribed in Eq. (32). Additionally, this characteristic renders the parameter selection less sensitive, facilitating robust contact enforcement.

Remark. From a numerical implementation perspective, to ensure that the barrier energy and the associated contact pressure approach infinity as the gap closes when employing the barrier method, the temporal resolution must be sufficiently high to capture the sharp gradient. This treatment, however, inevitably increases the overall computational cost. In the current study, we have implemented a simple yet effective adaptive time step, i.e., $\Delta t = \min(\min(\bar{g}_k)/g_c, 1)\Delta t^0$ for addressing this issue. Despite its simplicity, this approach has demonstrated an efficacy in balancing computational costs and accuracy, making it a practical solution for complex contact problems.

3.4.2. Tangential frictional behavior

In this work, frictional contact is considered. The tangential contact behavior is described using Coulomb's friction law, which can be expressed as:

$$\lambda^\tau \leq \mu \lambda^n, \tag{49}$$

where μ is the friction coefficient. When the tangential stress is less than the allowable (slip) frictional stress, the contact surface will be in a sticking state. Here, we utilize the simplest penalty method to constrain relative sliding, and Eq. (49) can be rewritten as:

$$\lambda^\tau = \min(\kappa_\tau u_\tau, \mu \lambda^n) \tag{50}$$

where κ_τ is the contact stiffness along the tangential direction, and u_τ represents the sliding displacement. For u_τ, it can be computed similarly to the weighted gap distance shown in Eq. (40) and (46), but in an incremental form:

$$\begin{aligned}\dot{u}_k^\tau &= \boldsymbol{\tau}_k \cdot \left[\sum_{i=1}^{n_p^s} \int_{\Gamma_c^s} N_k(\boldsymbol{x}_s) N_i(\boldsymbol{x}_s) \dot{\boldsymbol{u}}_i \mathrm{d}\Gamma - \sum_{j=1}^{n_p^m} \int_{\Gamma_c^s} N_k(\boldsymbol{x}_s) N_j(\bar{\boldsymbol{x}}_m) \dot{\boldsymbol{u}}_j \mathrm{d}\Gamma\right] \\ &= \boldsymbol{\tau}_k \cdot \left[\sum_{i=1}^{n_v^s} D_{ki} \dot{\boldsymbol{u}}_i - \sum_{j=1}^{n_v^m} M_{kj} \dot{\boldsymbol{u}}_j\right], \quad k \in [1, 2, \ldots, n_v^s]\end{aligned} \tag{51}$$

3.4.3. Contact force mapping

Upon determining the contact pressure for the contact surfaces, represented as $\lambda = \lambda^n \boldsymbol{n} + \lambda^\tau \boldsymbol{\tau}$, the next step involves computing the equivalent contact forces acting on the boundary vertices on the slave and the master surfaces, which can be accomplished via the contact virtual work. In the current configuration, the contact virtual work is written as:

$$\delta \Pi_c(\boldsymbol{u}, \delta \boldsymbol{u}, \lambda) = \int_{\Gamma_c^s} \lambda \cdot (\delta \boldsymbol{u}_s - \delta \boldsymbol{u}_m) \mathrm{d}\Gamma \tag{52}$$

Substituting the discretization of gap distance (Eq. (37)) into the above expression, the contact virtual work is written as:

$$\begin{aligned}&\delta \Pi_c(\boldsymbol{u}, \delta \boldsymbol{u}, \lambda) \\ &= \sum_{i=1}^{n_v^s} \left[\sum_{k=1}^{n_v^s} \int_{\Gamma_c^s} N_k(\boldsymbol{x}_s) N_i(\boldsymbol{x}_s) \lambda_k \mathrm{d}\Gamma\right] \delta \boldsymbol{u}_i - \sum_{j=1}^{n_v^m} \left[\sum_{k=1}^{n_v^s} \int_{\Gamma_c^s} N_k(\boldsymbol{x}_s) N_j(\bar{\boldsymbol{x}}_m) \lambda_k \mathrm{d}\Gamma\right] \delta \boldsymbol{u}_j \\ &= \boldsymbol{\mathcal{F}}_c^s \delta \boldsymbol{u}_s - \boldsymbol{\mathcal{F}}_c^m \delta \boldsymbol{u}_m\end{aligned} \tag{53}$$

with

$$\boldsymbol{\mathcal{F}}_c^s = \boldsymbol{\mathcal{D}} \lambda, \tag{54}$$

$$\boldsymbol{\mathcal{F}}_c^m = \boldsymbol{\mathcal{M}}^T \lambda, \tag{55}$$

where $\boldsymbol{\mathcal{F}}_c^s \in \mathbb{R}^{n_v^s \times \mathrm{dim}}$ and $\boldsymbol{\mathcal{F}}_c^m \in \mathbb{R}^{n_v^m \times \mathrm{dim}}$ represent the vectors of forces acting on all boundary vertices on the slave and master surfaces, respectively (*i.e.*, $\boldsymbol{\mathcal{F}}_c^s = \left[\boldsymbol{f}_1^c, \boldsymbol{f}_2^c, \ldots, \boldsymbol{f}_{n_v^s}^c\right]^T$).

Finally, the vertex forces exerted on each body are mapped to their corresponding layer of background mesh via the augmented weighting function:

$$\boldsymbol{f}_I^{\mathrm{con}} = \sum_{k=1}^{n_v} \bar{S}_{Ik} \boldsymbol{f}_k^c \tag{56}$$

where $\boldsymbol{f}_I^{\mathrm{con}}$ denotes the nodal contact forces at node I, and $\boldsymbol{f}_k^c$ is the contact force at vertex k. With the nodal contact force, the nodal momentum equation (Eq. (17)) can be solved accordingly.

3.5. Multi-body contact

As the number of contacting bodies increases, the segment-to-segment contact detection method may become computationally demanding and hinder the overall performance. To address this limitation, we propose using the Axis-Aligned Bounding Boxes (AABB) algorithm, which is widely adopted in DEM [69–71], for broad-phase contact detection. Compared to the original AABB algorithm, we construct an expanded AABB for each body $\mathcal{B}$ to account for a critical gap g_c introduced in the barrier method. The expanded AABB for a body $\mathcal{B}$ is defined as follows:

$$AABB(\mathcal{B}) = \left\{ \left[\min_x(\mathcal{B}) - \frac{1}{2}g_c, \max_x(\mathcal{B}) + \frac{1}{2}g_c\right], \left[\min_y(\mathcal{B}) - \frac{1}{2}g_c, \max_y(\mathcal{B}) + \frac{1}{2}g_c\right] \right\}. \tag{57}$$

After constructing the AABBs for all bodies, the overlap test is performed. If $\mathcal{B}_s$ and $\mathcal{B}_m$ overlap on all two axes, they are considered potentially in contact, and the aforementioned segment-to-segment approach is invoked for a more precise detection. Employing the expanded AABB method significantly enhances computational efficiency by reducing the number of detailed analyses required, particularly in scenarios with numerous bodies, as demonstrated in our last numerical experiment (Section 4.6).

3.6. Computational procedure

The computational procedure for the proposed contact algorithm is summarized in Algorithm 2 as shown below:

Algorithm 2 Computational procedure of segment-to-segment frictional contact in MPM

if $t = 0$ **then**
  Initialize material points and boundary vertices.
end if
while $0 < t < t_{\text{end}}$ **do**
  Material point to grid interpolation, (Eqs. (4)–(6)).
  Weighting function augmentation for boundary vertex, (Eq. (27)).
  Update particle state variables, *e.g.*, strain and stress, (Eqs. (10)–(16)).
  if Pass broad-phase contact detection (Section 3.5) **then**
    Segment-to-segment contact detection and obtain gap distance, (Eqs. (46) and (51)).
    Apply contact constraints and get contact pressure, (Eqs. (50), (54)–(55)).
    Map vertex contact forces to grid nodes, (Eq. (56)).
  end if
  Solve the motion equations on the background mesh, (Eq. (17)).
  Update kinematics and positions for particles, (Eqs. (21)–(24)).
  Update kinematics and positions for boundary vertex, (Eqs. (29)–(30)).
end while

4. Numerical examples

In this section, we will examine the overall capability of the proposed framework through five numerical examples with increasing complexity, with each focusing on a specific aspect of the proposed algorithm. These examples include the elastic cantilever beam, Hertz contact problem, disk on an inclined plane, collision of two rings, ironing test, and compaction of soft grain packing. Some simulation animations can be found at https://github.com/WeijianLiang/mpm-mortar-contact.

4.1. Elastic cantilever beam

Prior to discussing the contact algorithm in detail, we first verify the accuracy of the MPM framework by the well-studied elastic cantilever beam [40,72], placing particular emphasis on the weighting function augmentation and the kinematic updating scheme for boundary vertices.

The model setup is shown in Fig. 5. The beam is 4 m in length and 1 m in height, and it is discretized into 64 quadrilateral elements with an element width of $h = 0.25$ m. Each element consists of 9 material points (PPC = 9). The beam is modeled using a linear elastic material with the following properties: Young's modulus $E = 10^6$ Pa, Poisson's ratio $\nu = 0.3$, density $\rho = 1050$ kg/m^3, and a simulated time of $t = 3$ s. The gravitational acceleration is $\|\boldsymbol{g}\| = 10.0$ m/s^2. The damping coefficient α_{damp} is set to 0, and the PIC fraction α_{pic} is also 0. For verification purpose, we also conduct FEM analysis under the same conditions using the commercial FEM package Abaqus taking large deformations into account.

Fig. 6 illustrates the vertical deflection of the lower-rightmost material point of the beam. While there is a minor discrepancy against FEM, mainly resulting from differences in the positions of the monitored points, the MPM provides a satisfied prediction. This is particularly evident when compared with the CPDI results from [40], indicating the desired accuracy of the overall code.. Due to

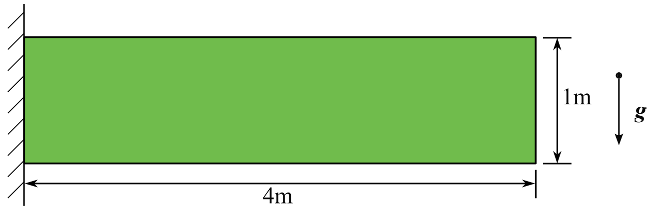

Fig. 5. Model setting for the elastic cantilever beam problem.

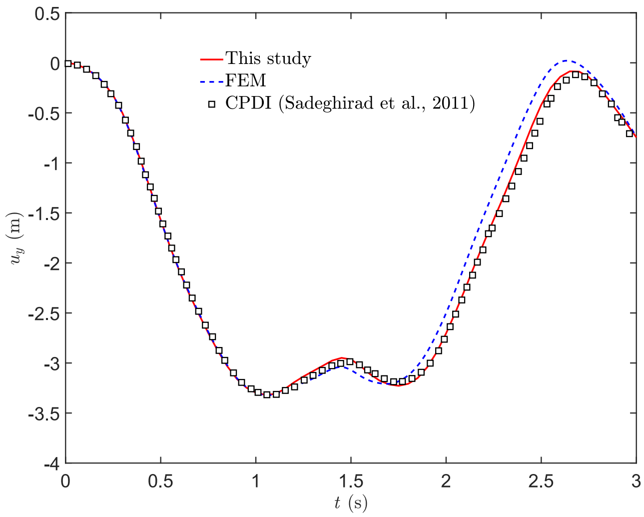

Fig. 6. Vertical deflection for the lower-right most material point.

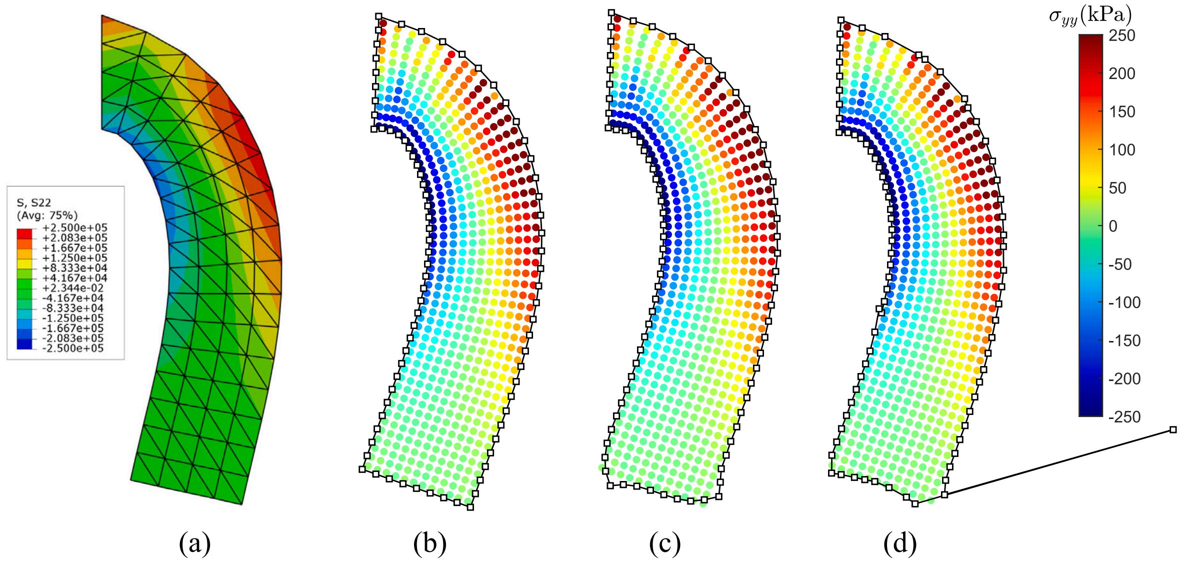

Fig. 7. Contour of vertical stress, σ_{yy}, and boundary vertex positions for the cantilever beam at t = 1.5 s: (a) FEM (Abaqus) result, (b) MPM with weighting function augmentation and affine-type kinematic update, (c) MPM with weighting function augmentation, (d) MPM with affine-type kinematic update.

the absence of external traction, the evolution of vertex configuration does not affect the position of material points. Consequently, the simulation results without weighting function augmentation or affine kinematic update are not presented for brevity.

Fig. 7 shows the contour of vertical stress σ_{yy} and the boundary vertex positions for the cantilever beam at t = 1.5 s. Specifically, we focus on how the vertex configuration is influenced by weighting function augmentation and affine-type kinematic

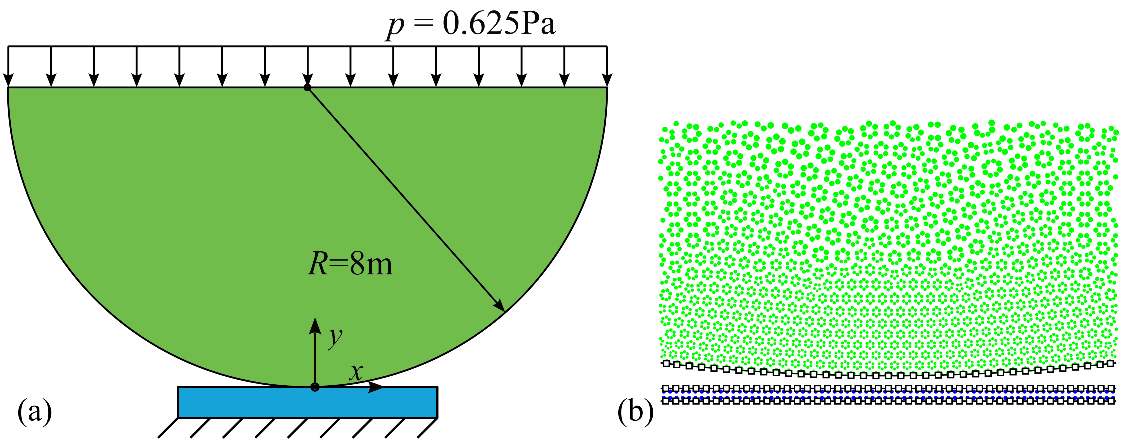

Fig. 8. Model setting for two-dimensional Hertz contact problem: (a) geometry, and (b) discretization around the contact region.

updates. As can be observed, weighting function augmentation and affine-type kinematic updates are essential for maintaining the conforming geometry evolution between boundary vertices and the internal material points, particularly in problems involving large deformations and rotations. Omitting weighting function augmentation (Fig. 7(d)) would induce significant errors in vertex positioning, as indicated by the irregular intervals between vertices on the top surface of the beam and the scattered vertices that deviate from the main body. This discrepancy is attributed to the violation of the partition of unity for the vertices, especially those located on the rear side of the beam, which become increasingly distant from the main body and eventually locate beyond the support domain of all material points. In contrast, the impact of neglecting the affine-type kinematic update is less severe, primarily affecting the vertices at the corners, which exhibit a noticeable delay in their swinging motion. The proposed affine-type kinematic update properly accounts for the local affine velocity field, thus ensuring a more accurate representation of the beam boundary, particularly at the corners where large rigid rotations occur.

4.2. Hertz contact problem

We then proceed to verify the proposed contact scheme in the small deformation regime using the classical Hertz contact problem. The model setup for the Hertz contact problem is illustrated in Fig. 8, where a semicircle of radius R is positioned above a flat surface. The top surface of the semicircle is subjected to a constant pressure p. Under the assumption of small displacement, the normal contact pressure p_c and the width of the contact area b are determined according to [73] as follows:

$$p_c = \frac{4Rp}{\pi b^2}\sqrt{b^2 - x^2}, \tag{58}$$

$$b = 2\sqrt{\frac{2R^2 p(1-\nu^2)}{E\pi}}, \tag{59}$$

where E and ν are the Young's modulus and Poisson's ratio, respectively, while x denotes the position along the x-axis with the origin at the contact point between the semicircle and the flat surface. In the current study, we select the simulation parameters specified in [50]. The radius of the semicircle is set to $R = 8$ m, with an applied pressure $p = 0.625$ Pa on the upper surface, ensuring compliance with the small deformation criterion. The linear elastic model is adopted with the following material properties: $E = 200$ Pa and $\nu = 0.3$. Under such setting, the width of the contact area is calculated as $b = 0.681$ m [73]. To accurately capture the behavior in areas of concentrated strain, we carry out a finer discretization (more material points) around the contact area as shown in Fig. 8(b). The whole semicircle comprises a total of 49,332 material points, with an average vertex segment size of 0.04 m. The background mesh size is $h = 0.1$m. To mitigate stress oscillation during contact, we introduce a small damping with $\alpha_{\text{damp}} = 0.01$ and a PIC value $\alpha_{\text{pic}} = 0.1$. For the contact algorithm, the initial gap between the semicircle and the bottom body is $g_0 = 0.05$, the critical gap for contact detection is $g_c = 0.05$, and the contact stiffness coefficient is $\kappa = 1500$. Friction is not considered in this simulation, and the simulation is terminated when $t = 50$ s.

Fig. 9 presents a comparison of the contact pressure distribution obtained from the numerical simulation and the analytical solution. While minor discrepancies are observed at the boundary of the contact area, attributable to mesh and particle resolution, the numerical results show good agreement with the analytical solution. Fig. 10 shows the contours of vertical displacement u_y and vertical stress σ_{yy}. The smoothness of these contours collectively indicates the robustness of the proposed schemes, being free of numerical instability. Notably, the stress contour reveals a concentrated stress profile, with the maximum value located at the center of the contact area. This peak in stress diminishes symmetrically towards both ends, aligning well with the predictions of Hertzian contact mechanics. This example effectively demonstrates the capability of the proposed contact scheme to accurately capture pressure distributions during contact.

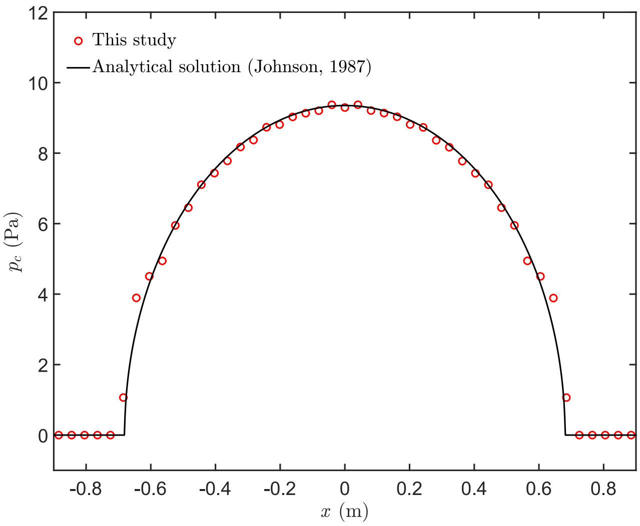

Fig. 9. Comparison of contact pressure between numerical simulation and analytical solution [73].

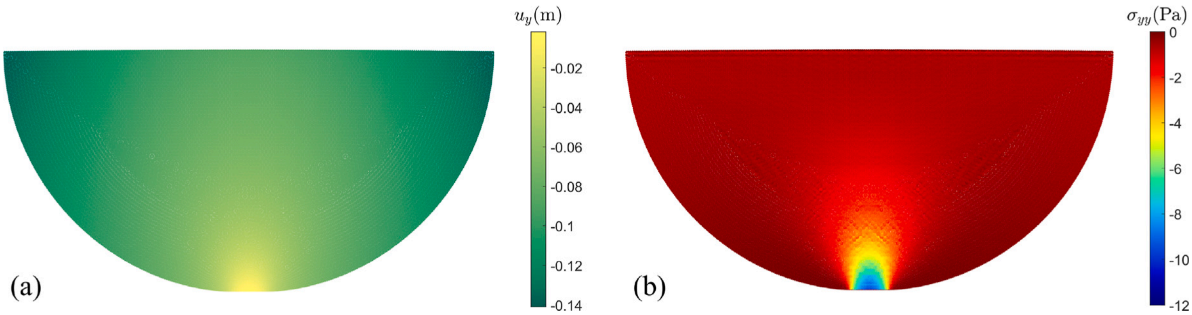

Fig. 10. Contour of (a) vertical displacement u_y, and (b) vertical stress σ_{yy}, at the final state.

4.3. Disk on inclined plane

We advance our verification of the proposed contact algorithm within dynamic scenarios. Here, we revisit another classical example where a rigid disk is positioned on an inclined plane. Upon commencement, the disk may either roll down the inclined plane with or without slippage, depending on the inclination angle of the plane θ and the coefficient of friction μ. Specifically, the transition between pure rolling (stick) and rolling with slipping (slip) is determined by the inequality condition: $\tan(\theta) > 3\mu$. If this condition is satisfied, it means the slope is too steep, and the disk will undergo a composite motion consisting of both rolling and slipping. Conversely, if the condition is not met, the disk will maintain a pure rolling motion without any slippage. For both scenarios, the horizontal displacement of the disk (measured at the center of mass), u_x, can be quantified as a function of time [29] as:

$$u_x = \begin{cases} \frac{1}{2}\|\boldsymbol{g}\|t^2(\sin\theta - \mu\cos\theta), & \text{for slip}, \ \tan\theta > 3\mu \\ \frac{1}{3}\|\boldsymbol{g}\|t^2\sin\theta, & \text{for stick}, \ \tan\theta \le 3\mu \end{cases} \tag{60}$$

where $\|\boldsymbol{g}\|$ denotes the magnitude of gravity.

The simulation setup is depicted in Fig. 11. A disk with a radius of $R = 0.5$ m is positioned on a plane inclined at an angle $\theta = 30°$ to the horizontal. The gravitational acceleration is set to $\|\boldsymbol{g}\| = 9.81$ m/s^2. For ease of simulation, the x-axis is aligned parallel to the plane orientation while the y-axis is orthogonal to it. The linear elastic model is adopted for both the disk and the inclined plane, with a Young's modulus of $E = 250$ kPa, a Poisson's ratio of $\nu = 0.3$, and a density $\rho = 300$ kg/m^3. These parameters are selected to prevent excessive deformation at the contact zone, which could result in undesired rolling resistance and influence the comparison with the analytical solution. The background mesh size is $h = 0.1$ m. The disk is discretized by 2236 material points and 64 vertices, with an average segment size of 0.05 m. The PIC value is set to $\alpha_{\text{pic}} = 0.001$, and no damping is applied. The critical gap for contact is $g_c = 0.04$ m, and the initial gap is $g_0 = 0.02$ m. The friction coefficient μ is taken as 0.1 or 0.3 for the slip and stick conditions, respectively. The contact stiffness parameters are $\kappa = 1 \times 10^4$ and $\kappa_t = 1 \times 10^6$. The simulation is performed in two

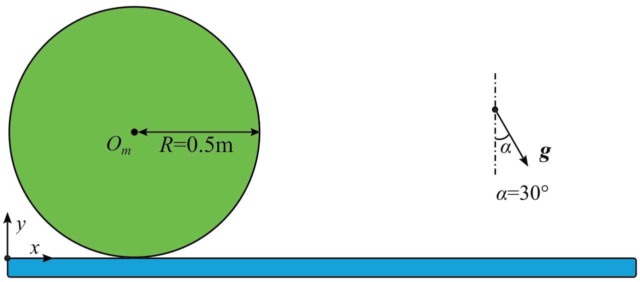

Fig. 11. Model setting for modeling a disk on inclined plane.

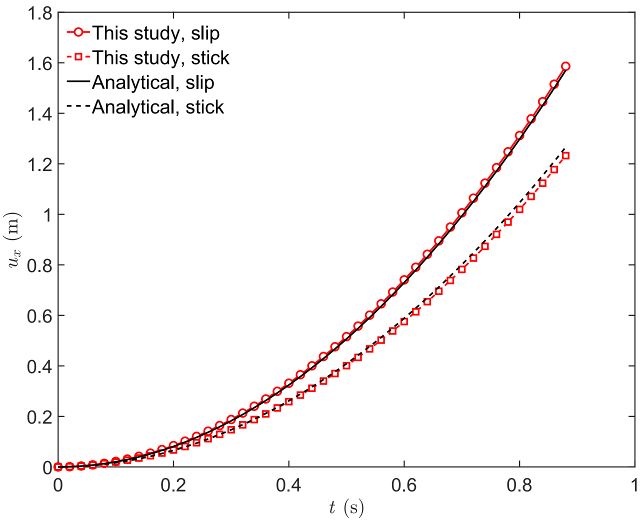

Fig. 12. Displacement along x direction for slip and stick conditions (the analytical solution is from Ref. [29]).

stages: initially, only the y-axis component of gravity is applied to achieve an equilibrium stress state, and in the second stage, both x- and y-axis components of gravity are activated. This approach helps to prevent rebounding of the disk on the inclined surface during mobilization, in compliance with the analytical solution assumption.

Fig. 12 depicts the evolution of the displacement along the x-axis, u_x, for both friction regimes. The simulation results match well with the analytical solutions for both stick and slip conditions, accurately capturing the gradual acceleration of the disk. Fig. 13 presents snapshots of the velocity field, $\boldsymbol{v}$, at $t = 1.8$ s, providing insight into the kinematic behavior under varying frictional conditions. In the slip condition, the velocity is distributed more uniformly across the disk, and its direction of mobilization is more aligned with the inclined plane, emphasizing the dominant translational motion. In contrast, in the stick condition, the disk undergoes pure rolling motion, with the rolling center located at the contact point between the disk and the inclined plane. This numerical example again showcases the robustness of the proposed contact scheme under different frictional conditions.

4.4. Collision of two elastic rings

The two preceding numerical examples have showcased the effectiveness of the proposed contact algorithm for MPM within the small deformation regime. This example focuses on large deformation scenarios and involves the collision of two elastic rings. This example is initially designed to highlight the potential tensile instability issue in SPH [74,75], and has subsequently been widely adopted to evaluate the overall performance of various contact algorithms [32,46,76] and the numerical stability of new schemes [2,77].

The model setup is illustrated in Fig. 14, with dimensions taken from [76]. The two identical rings are modeled using a compressible Neo-Hookean material under plane strain conditions, with a bulk modulus $K = 121.7$ MPa, shear modulus $G = 26.1$ MPa, and density $\rho = 1010$ kg/m^3. The background mesh size is $h = 0.1$ m. Each ring is discretized using 4056 material points, and its outer boundary is discretized using 127 vertices, with an average segment size of 6.9×10^{-3} m. The PIC value is set to $\alpha_{\text{pic}} = 0$, and no damping is applied to avoid excessive energy dissipation. The critical gap for contact is $g_c = 5 \times 10^{-3}$ m. The friction coefficient μ is taken as 0.1. The contact stiffness parameters are set as $\kappa = 4 \times 10^7$ and $\kappa_t = 1 \times 10^6$.

Fig. 15 presents snapshots of the mean stress σ_m at various time instances, while Fig. 16 shows the evolution of the contact force throughout the collision. It is clear that the two rings collide at $t = 0.25$ ms and separate at $t = 3.25$ ms, with the contact force

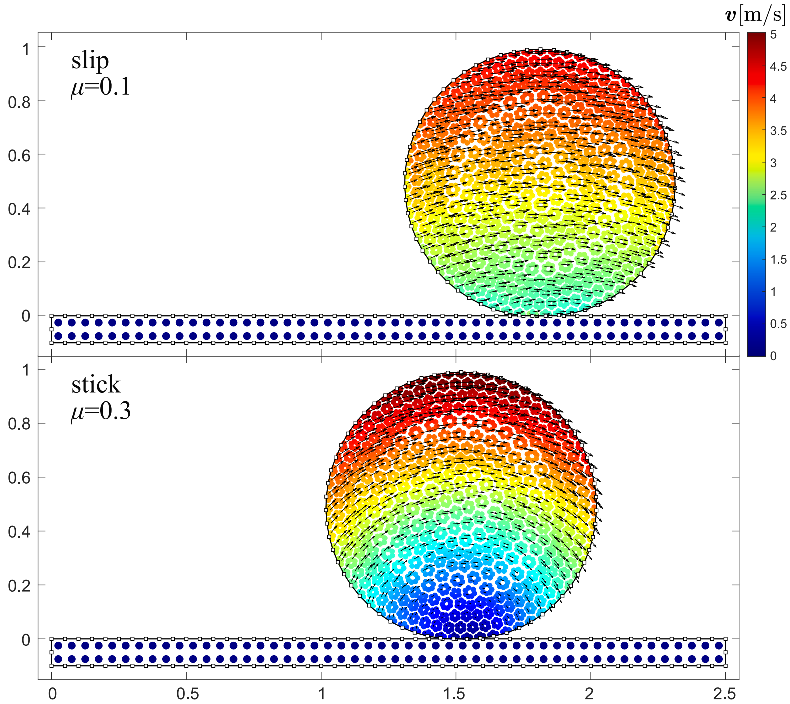

Fig. 13. Contour of velocity field, $\boldsymbol{v}$ for slip and stick conditions at $t = 1.8$ s (the arrow indicates the direction of the velocity).

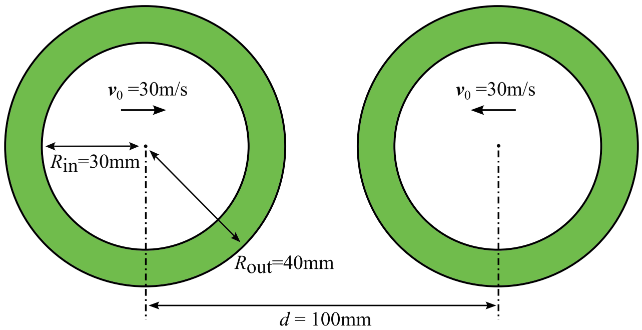

Fig. 14. Model setting for modeling the collision of two elastic rings.

reaching up to 250 kN. The overall deformation pattern is qualitatively consistent with the results obtained using the generalized particle in cell method for the same problem [76]. Notably, the gap between the two rings during the collision is narrower than that reported by [76] (which is not shown here), despite using the same background mesh size. This difference is mainly attributed to the fact that, in the current study, the proposed algorithm relies on the boundaries of the two bodies rather than the background mesh for contact detection.

We also track the time history of energy transfer during the collision process, as shown in Figure 17, where kinetic energy is defined as $E_k = \frac{1}{2}\sum_p m_p \boldsymbol{v}_p^2$, strain energy as $E_s = \frac{1}{2}\sum_p V_p \boldsymbol{\sigma}_p : \boldsymbol{\epsilon}_p$, and total energy as $E_t = E_k + E_s$. The current research exhibits good agreement with the FEM results by [76] for both E_k and E_s, while showing some discrepancy in the total energy E_t. This discrepancy is primarily due to the fact that the FEM also considers hourglass energy in this problem.

4.5. Ironing test

In this subsection, we model an ironing test to evaluate the performance of the proposed algorithm under conditions of large deformation and sliding. This numerical example is widely adopted in the literature [47,49,50,78].

The geometry and boundary conditions of the model are shown in Fig. 18(a). The soft block is 12 m in width and 4 m in height. The bottom surface of the soft block is fixed. A rigid indenter, composed of a 2 m × 1 m rectangle and a semicircle with a radius

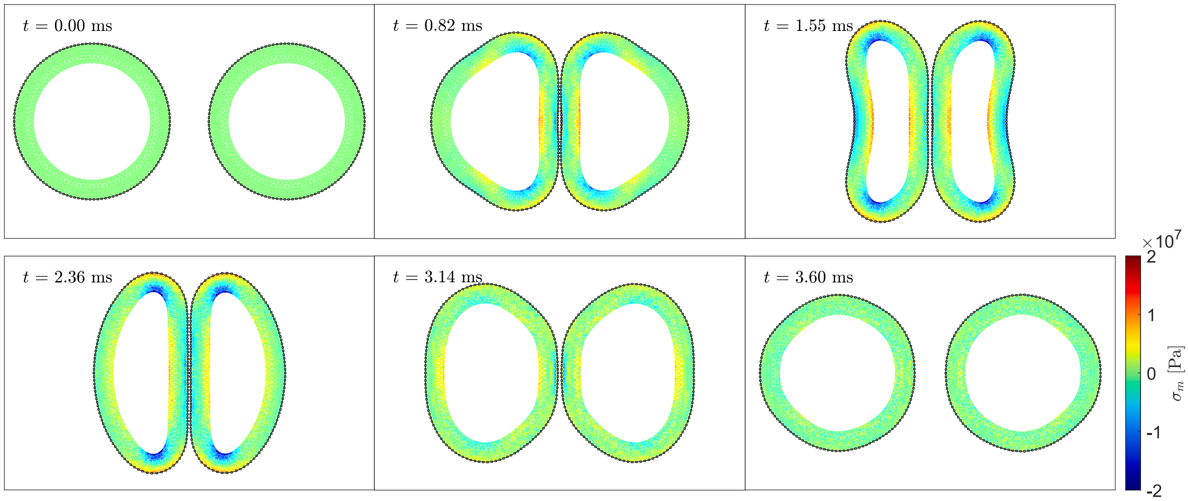

Fig. 15. Snapshots of mean stress σ_m at various time instances during the collision.

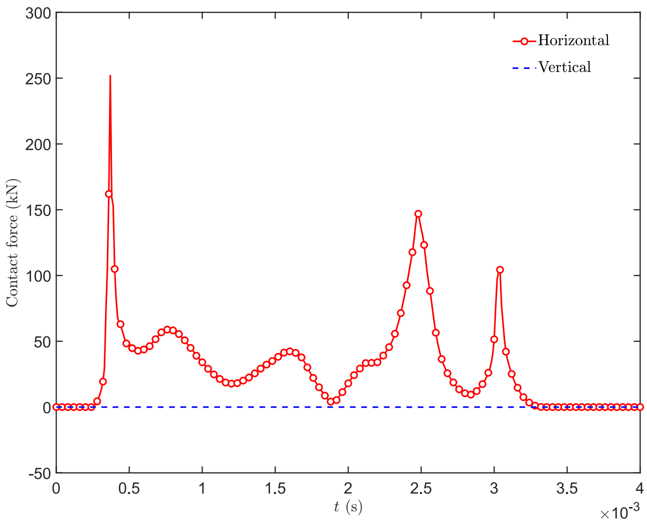

Fig. 16. Contact force evolution.

$R = 1$ m, is positioned 0.2 m above the elastic block and 0.2 m from the left edge of the block. During the simulation, the indenter is first pressed to a depth of 1.0 m into the block, and subsequently displaced horizontally towards the right edge until it leaves the block. The prescribed velocity for the indenter is delineated in Fig. 18(b). To avoid undesired impulse-induced stress, the velocity is ramped at the early stage of the loading. In this study, the block is simulated using a linear elastic model with a Young's modulus of $E = 600$ kPa, a Poisson's ratio of $\nu = 0.32$, and a density of $\rho = 2000$ kg/m^3. The density is selected to be relatively large to permit larger time steps. The background mesh size is $h = 0.2$ m. The block is represented by 10,800 material points, while the indenter is discretized by 1809 material points. The average segment size for vertices is 0.1 m. The PIC parameter α_{pic} is set to 0.1, and damping coefficient α_{damp} is set to 0.05. The contact stiffness parameters are $\kappa = 1000$ and $\kappa_t = 1 \times 10^4$. The critical contact gap is set as $g_c = 0.04$ m, and the friction coefficient μ is examined at values of 0.1 for the frictional case and 0 for the frictionless case.

Fig. 19 presents the reaction force exerted on the indenter over time. As highlighted by previous analyses [49,50], discrete contact detection, particularly in particle-based numerical methods, can lead to significant oscillations in contact forces in ironing problems, potentially resulting in convergence issues or computational failures. Notably, the proposed contact algorithm, which conducts contact detection in a segment-to-segment weak form, yields a stable reaction force without significant oscillations under both frictional and frictionless conditions. For the vertical reaction force, both frictional and frictionless cases yield nearly identical results, with the vertical reaction force rapidly rising to 500 N during the initial phase of pressing the indenter into the soft block. As the indenter moves horizontally, the vertical reaction force increases slightly before stabilizing. As the indenter approaches the right edge of the block, the vertical reaction force quickly drops to zero. Conversely, the horizontal reaction force is significantly

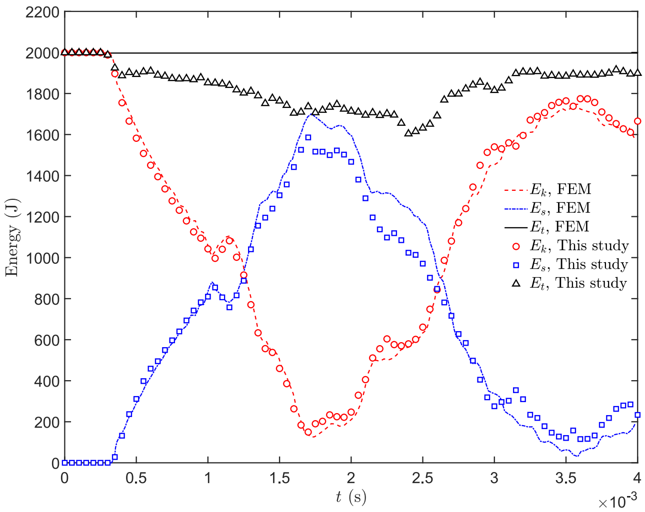

Fig. 17. Energy evolution during the collision. The FEM results are extracted from [76], where the total energy E_t includes not only the kinetic energy E_k and strain energy E_s, but also the hourglass energy.

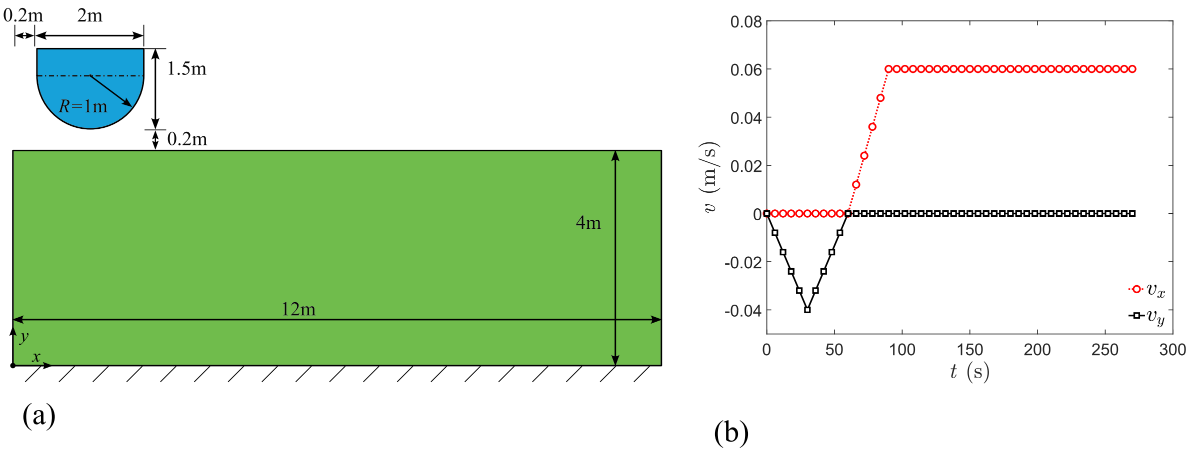

Fig. 18. Model setting for the ironing test: (a) geometry and boundary conditions; (b) prescribed velocity of the indenter.

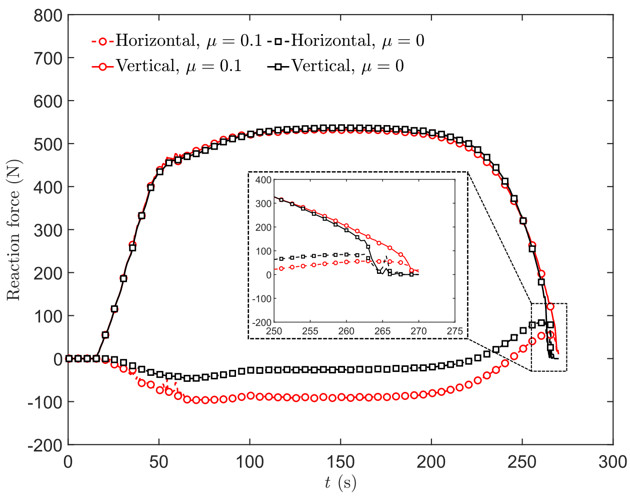

Fig. 19. Reaction force exerted at the indenter.

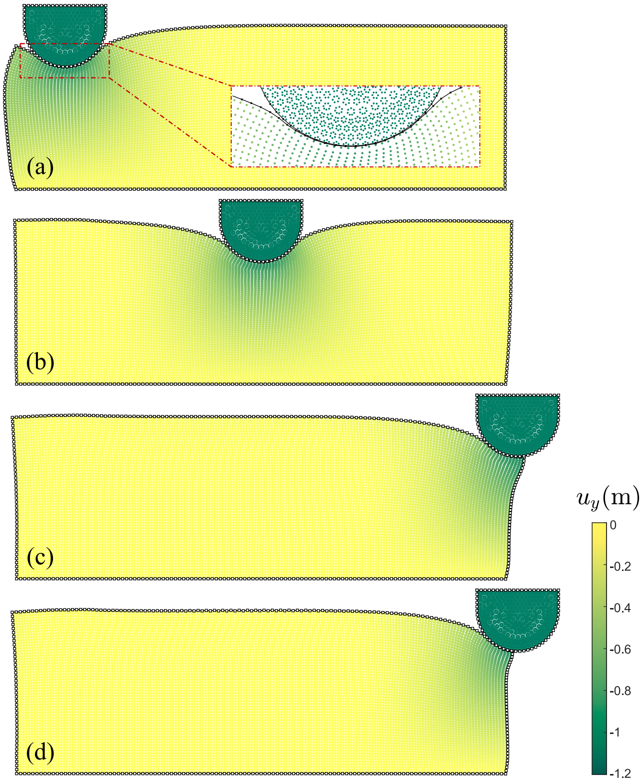

Fig. 20. Contour of vertical displacement, u_y, during the loading process: (a) t = 60 s, $\mu = 0.1$; (b) t = 155 s, $\mu = 0.1$; (c) t = 260 s, $\mu = 0.1$; (d) t = 260 s, $\mu = 0$.

smaller than the vertical one, and friction causes a considerable difference in the horizontal force. In the frictionless case, despite the absence of friction, a leftward reaction force is generated due to the rightward motion of the indenter. In the case with friction, the horizontal reaction force is comparatively larger due to the additional frictional resistance. Interestingly, as the indenter is about to depart from the soft block, the elastic block experiences a leftward slippage under the compression of the indenter, generating a leftward reaction force, which is more pronounced in the frictionless case (as can be observed from Figs. 20(c) and (d)).

Fig. 20 presents snapshots of the vertical displacement at various time instances and friction coefficients. The simulation effectively captures the deformation of the soft block, with no signs of instability observed throughout. For the frictionless case, the slippage of the soft block is clearly observed (Figs. 20(c) and (d)). Specifically, the detailed view in Fig. 20(a) illustrates the configuration of the indenter and the block in the contact area, showing that the soft block deforms in a manner conforming to the shape of the indenter, with a smooth transition between the deformed and undeformed regions. Additionally, the gap between the indenter and the soft block is significantly smaller than the grid size h, without showing any mesh dependency issues that is commonly encountered in prior grid-based contact algorithms. Furthermore, despite the close proximity of the contact surfaces, no penetration occurs due to the rapidly increasing contact force facilitated by the adoption of the barrier method (see Fig. 4). This characteristic highlights the superior performance of the kinematic update scheme for vertices and the proposed contact algorithm in maintaining accuracy irrespective of the mesh resolution. Fig. 21 presents the contours of vertical and shear stresses, σ_{yy} and σ_{xy}, at $t = 155$ s. Despite minor oscillations beneath the indenter, the overall stress distribution remains stable and smooth. For σ_{xy}, the active side of the block undergoes greater shearing due to the rightward movement of the indenter.

4.6. Compression of deformable grain packing

To further demonstrate the effectiveness of the proposed contact algorithm in handling multi-body contact, we simulate the compaction of a soft grain packing. Similar problems are also investigated by [44,79,80]. The model setup for the compaction simulation is shown in Fig. 22, where Fig. 22(a) depicts the geometry and boundary conditions, and Fig. 22(b) shows the initial discretization for all involved grains. In the simulation, 16 irregularly shaped deformable grains are positioned inside a container with dimensions of 10 × 13 m, with a rigid loading plate at the top. Notably, all grains have varying shapes, with some featuring concave geometries. This setting also implies that multiple pairs of contacts could simultaneously occur between neighboring grains. Gravity is not taken into consideration, and grains are not in contact with each other initially. As will be demonstrated later, this setup leaves sufficient space for particle rearrangement and thus purposely showcases the capability of the proposed framework in

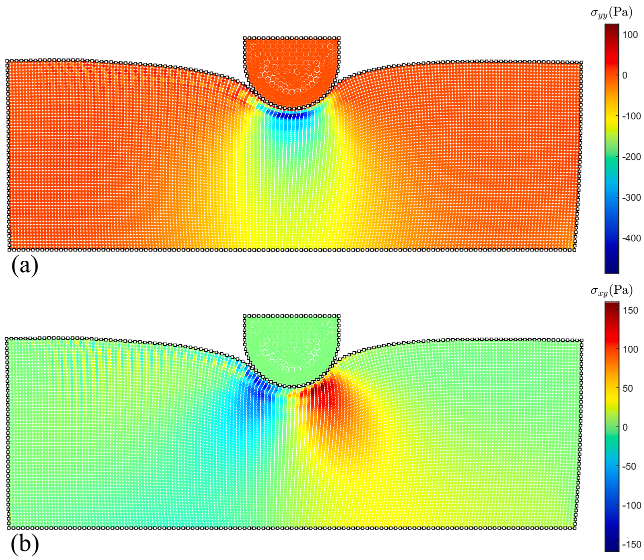

Fig. 21. Contour of stresses for the ironing process during $t = 155$ s: (a) σ_{yy}; (b) σ_{xy}.

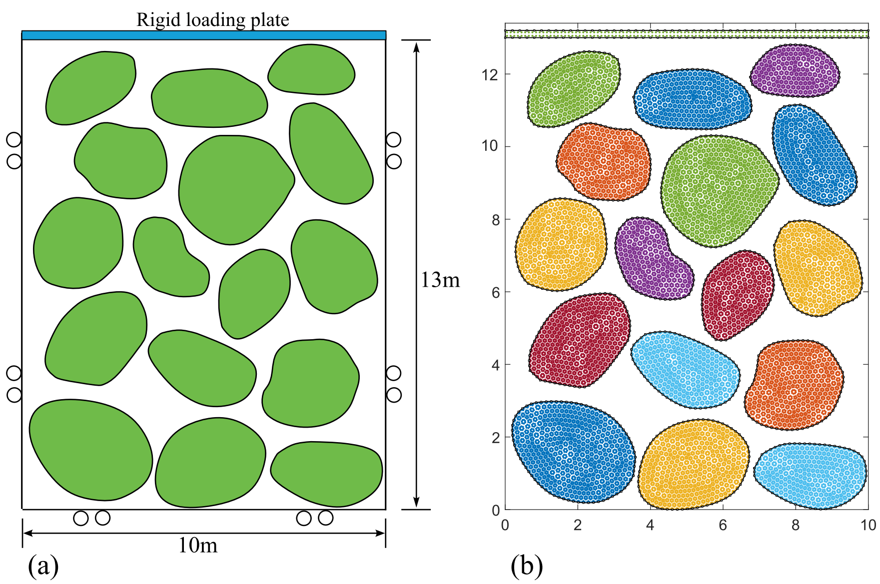

Fig. 22. Model setting for modeling the compaction of deformable grains packing: (a) geometry and boundary conditions, (b) discretization of sixteen deformable grains and the loading plate.

modeling complex particle motion and interaction. As the simulation commences, the rigid loading plate is moved downward with a constant velocity $v = 0.1$ m/s from the top, gradually compacting the grain assembly. The lateral and bottom boundaries of the container are modeled as frictionless walls, which restrict normal displacement but allow for tangential movement.

The linear elastic model with the following parameters is adopted for all grains: Young's modulus $E = 60$ kPa, Poisson's ratio $\nu = 0.32$, and density $\rho = 500$ kg/m^3. The element size of the background mesh is $h = 0.2$ m and the average particle size is 0.054 m, resulting in a total of 26,916 material points. The average segment size for the boundary vertices is 0.1 m. To ensure numerical stability and mitigate stress oscillations during grain collisions, we select a PIC parameter $\alpha_{\text{pic}} = 0.1$ and a damping coefficient $\alpha_{\text{damp}} = 0.1$. The critical contact gap is defined as $g_c = 0.085$ m, and the normal and tangential contact stiffness coefficients are set to $\kappa = 7 \times 10^4$ and $\kappa_t = 1 \times 10^5$, respectively. A friction coefficient $\mu = 0.2$ is used between grains as well as between the grains and the loading plate. The simulation is terminated when the loading plate reaches a maximum displacement of 0.49 m.

Fig. 23 presents the reaction force exerted on the loading plate during compression. The reaction force exhibits moderate fluctuations, which can be attributed to collisions among the grains and the propagation of stress waves within the material. Despite

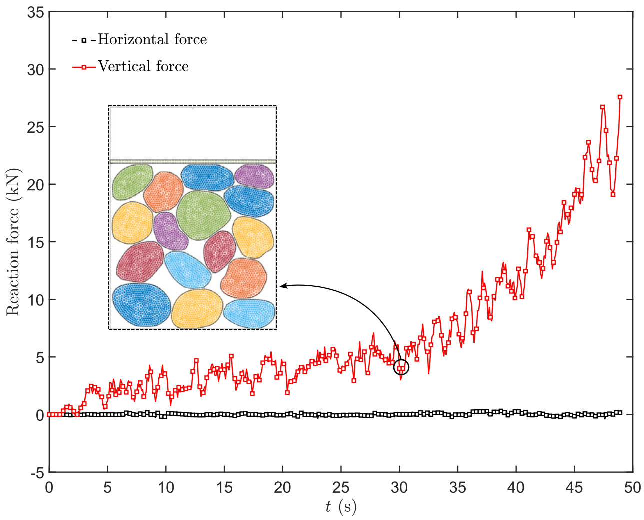

Fig. 23. Reaction force exerted on the loading plate.

these variations, the loading curve can be approximated by a bilinear curve, indicating two distinct phases of the compaction process. In the initial phase ($t < 30$ s), the slope of the curve is relatively gentle, suggesting that the early stage of compaction mainly involves the repositioning of grains with minimal resistance. During this period, the suspended grains are pushed downward and rearrange themselves without undergoing significant deformation, and the mobilized grains have not yet come into contact with the bottom of the container. After $t = 30$ s, the compacted grains reach the bottom of the container (as shown in the inserted configuration of the packing in Fig. 23), leading to the formation of a dense packing where the grains begin to interlock and deform to fill the voids between them. This results in a sharp increase in resistance. The pronounced change in slope marks a shift from the initial grain rearrangement to a phase dominated by grain deformation and load-bearing interactions. Conversely, the horizontal force stabilizes around zero throughout the compression process. Such a response is expected since the compaction process is primarily uniaxial, and the lateral boundaries are frictionless.

Fig. 24 presents snapshots of the stress fields, σ_{yy} and σ_{xy}, at displacements of $d = -0.25$ m and $d = -0.49$ m, along with the corresponding FEM results. At the early stage of loading, as the plate moves downward, force chains begin to form, transmitting the interaction forces. However, due to the sparse positioning of the grains, which allows for relatively free movement, the force chains are not fully developed, resulting in a noticeably heterogeneous stress distribution. As compaction enters the late stage ($t > 30$ s), the grains come into tight contact with the bottom of the container, enhancing the force chain network. The more interconnected force chains lead to a more uniform distribution of σ_{yy} across the grain packing, indicating that the grains are now behaving collectively, resisting the loading plate as a single unit rather than as individual grains. Meanwhile, the magnitude of σ_{xy} stress remains at a similar level as before, indicating the establishment of a stable grain structure with minimal sliding or shearing. In comparison to the FEM results, the structure of the packing, including the grain configuration and the force chain network, shows good agreement. However, the resulting stress is observed to be higher than that predicted by the FEM. This discrepancy primarily arises from the different contact enforcement approaches used in the two methods. In the current study, contact enforcement is implemented using the barrier method, which assumes a small gap between the contacting bodies and applies a repulsive force to prevent penetration. In contrast, the FEM relies on the penalty method, which allows for some overlap between the contacting bodies and determines the contact pressure based on the amount of penetration. This difference is particularly pronounced under conditions of compression with horizontal confinement. Furthermore, it is worth noting that the MPM result appears more fluctuated than that of the FEM. This is due to the combined effect of cell crossing noise and stress wave generation and rebounding. Implementing the Total Lagrangian MPM [43,81] could be a promising pathway for addressing this issue.

Fig. 25 presents a comparison of the displacement field against the FEM result at the final state of compaction ($d = -0.49$ m). As previously mentioned, the prepared packing has no initial contacts, providing enough space for particle rearrangement under the influence of multiple contacts with surrounding grains. Despite experiencing large rigid rotations, translations, and deformations, the current study demonstrates good agreement with the FEM results in the packing configuration. To further illustrate the complex motion that grains undergo during the compaction process, we track the configuration and velocity field of a representative grain, as shown in Fig. 26. The selected grain first rotates counterclockwise, navigating through the open spaces created by the two grains above. As the compaction process continues, it begins to fill the gap between them and effectively finds its way into a more stable position, coming into contact with the loading plate. Simultaneously, its top surface becomes flatter due to the pressure exerted by the loading plate pressing down upon it, reflecting the adaptability of the soft grain to external compression in a confined space and resulting in a compacted and stable grain structure. Despite significant deformation and a diverse range of motions, the algorithm can readily capture the contact interactions between the grains and with the loading plate, as well as the complex behaviors and shape changes of the grain with precision.

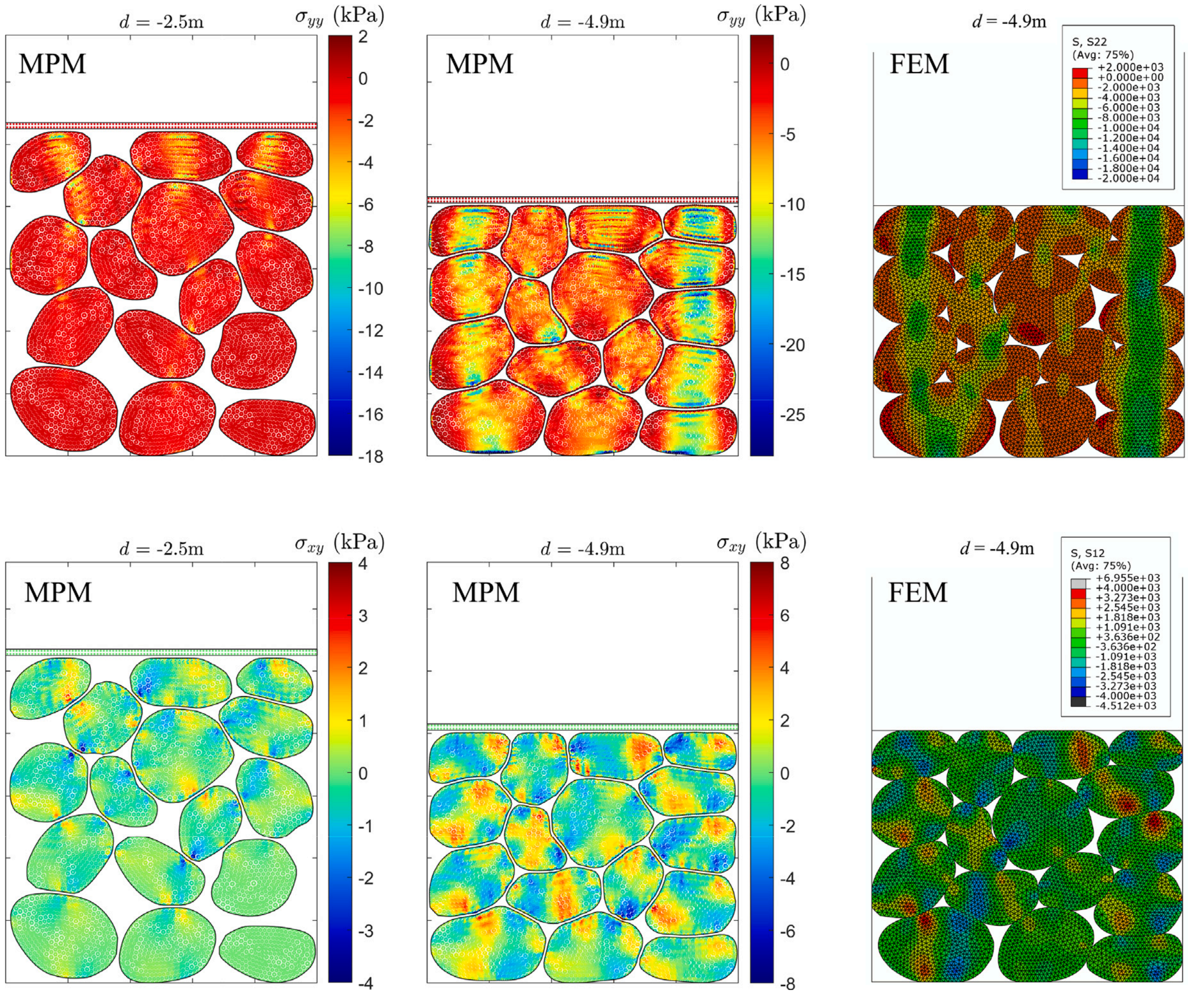

Fig. 24. Snapshots of stress field, σ_{yy} and σ_{xy}, during the compaction. The right column shows the FEM result at the final state $d = 0.49$ m.

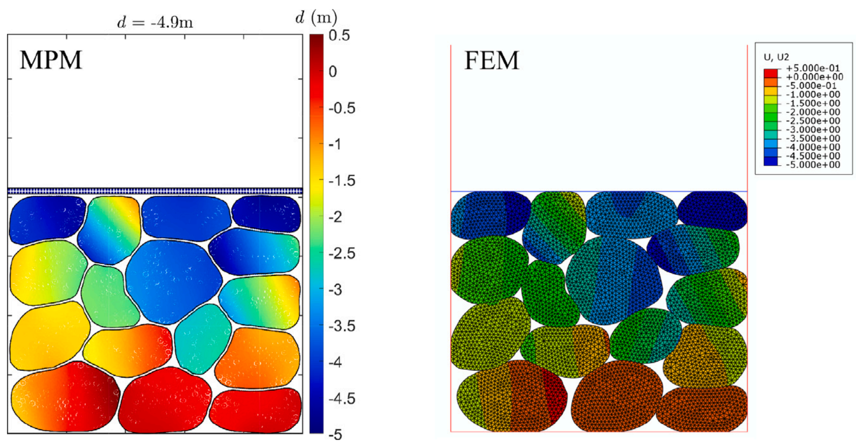

Fig. 25. Comparison of displacement field against FEM result at the final state of compaction $d = 0.49$ m.

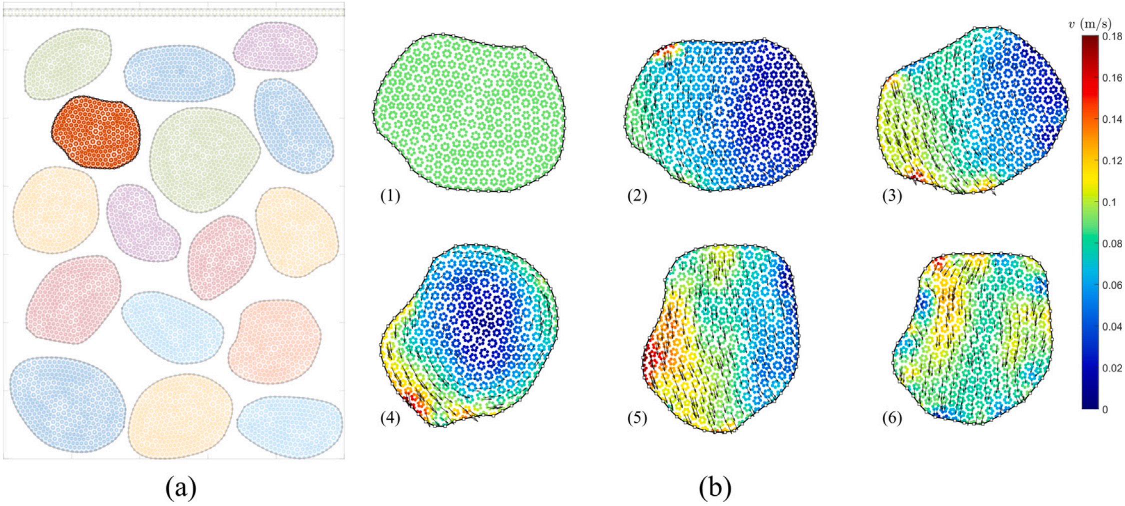

Fig. 26. (a) The initial position of the selected grain, (b) configuration and velocity field for the probed deformable grain.

5. Conclusion

In this study, we have developed a novel mortar segment-to-segment frictional contact approach for MPM to address limitations in traditional contact modeling techniques. Our proposed approach addresses these limitations by introducing boundary vertices to accurately represent the boundaries of the continuum media and their contact normals. We have also incorporated an augmented weighting function and a new kinematic update scheme to capture the dynamically evolving geometry. By utilizing the mortar method for segment-to-segment contact detection and an energetic barrier method for enforcing non-penetration conditions, our framework provides a robust solution capable of handling a wide range of contact scenarios, ranging from small to finite deformations that involve rolling, sliding, and multi-body contact interactions. We have demonstrated the effectiveness and versatility of our proposed contact algorithm through rigorous benchmark tests and complex applications, including the ironing test and compaction of soft packing, and highlighted the potential of our approach for broad engineering applications.

While our contact algorithm is effective for small to finite deformations, it may encounter challenges in scenarios involving massively large deformations, such as debris flows. In these cases, the configuration undergoes drastic changes, and severe distortion of boundary segments can lead to numerical instabilities and reduced accuracy. Future work will focus on extending our method to such regimes by adaptively refining and repositioning the boundary vertices. Additionally, the framework can be readily utilized to couple with FEM, offering a promising approach for modeling contact against thin wall structures, which is an ongoing study by the authors.

CRediT authorship contribution statement

Weijian Liang: Writing – review & editing, Writing – original draft, Software, Methodology, Formal analysis, Conceptualization. **Huangcheng Fang:** Writing – review & editing, Software, Methodology. **Zhen-Yu Yin:** Writing – review & editing, Supervision, Resources, Project administration, Funding acquisition. **Jidong Zhao:** Writing – review & editing.

Declaration of competing interest

The authors declare that they have no known competing financial interests or personal relationships that could have appeared to influence the work reported in this paper.

Data availability

Data will be made available on request.

Acknowledgments

This research is financially supported by the Research Grants Council (RGC) of Hong Kong Special Administrative Region Government (HKSARG) of China (Grant No.: 15220221, 15227923, 15229223) and the Start-up Fund for RAPs under the Strategic Hiring Scheme P0043929 from PolyU. The first author wishes to acknowledge fruitful discussions with Yidong Zhao of KAIST and Bodhinanda Chandra of UC Berkeley.

References

[1] D. Sulsky, Z. Chen, H.L. Schreyer, A particle method for history-dependent materials, Comput. Methods Appl. Mech. Engrg. 118 (1994) 179–196, http://dx.doi.org/10.1016/0045-7825(94)90112-0.
[2] D. Sulsky, S.-J. Zhou, H.L. Schreyer, Application of a particle-in-cell method to solid mechanics, Comput. Phys. Comm. 87 (1995) 236–252.
[3] E.J. Fern, K. Soga, The role of constitutive models in MPM simulations of granular column collapses, Acta Geotech. 11 (2016) 659–678, http://dx.doi.org/10.1007/s11440-016-0436-x.
[4] W. Liang, J. Zhao, Multiscale modeling of large deformation in geomechanics, Int. J. Numer. Anal. Methods Geomech. 43 (2019) 1080–1114, http://dx.doi.org/10.1002/nag.2921.
[5] W. Liang, S. Zhao, H. Wu, J. Zhao, Bearing capacity and failure of footing on anisotropic soil: A multiscale perspective, Comput. Geotech. 137 (2021) 104279, http://dx.doi.org/10.1016/j.compgeo.2021.104279.
[6] W. Liang, H. Wu, S. Zhao, W. Zhou, J. Zhao, Scalable three-dimensional hybrid continuum-discrete multiscale modeling of granular media, Internat. J. Numer. Methods Engrg. 123 (2022) 2872–2893, http://dx.doi.org/10.1002/nme.6963.
[7] J. Gaume, T. Gast, J. Teran, A. van Herwijnen, C. Jiang, Dynamic anticrack propagation in snow, Nature Commun. 9 (2018) 3047, http://dx.doi.org/10.1038/s41467-018-05181-w.
[8] J. Gaume, A. van Herwijnen, T. Gast, J. Teran, C. Jiang, Investigating the release and flow of snow avalanches at the slope-scale using a unified model based on the material point method, Cold Reg. Sci. & Technol. 168 (2019) 102847, http://dx.doi.org/10.1016/j.coldregions.2019.102847.
[9] X. Li, B. Sovilla, C. Jiang, J. Gaume, The mechanical origin of snow avalanche dynamics and flow Regime transitions, Cryosphere Discuss. (2020) 1–25, http://dx.doi.org/10.5194/tc-2020-83.
[10] A. Stomakhin, C. Schroeder, L. Chai, J. Teran, A. Selle, A material point method for snow simulation, ACM Trans. Graph. 32 (2013) 1, http://dx.doi.org/10.1145/2461912.2461948.
[11] H. Askari, K. Kamrin, Intrusion rheology in grains and other flowable materials, Nature Mater. 15 (2016) 1274–1279, http://dx.doi.org/10.1038/nmat4727.
[12] S. Dunatunga, K. Kamrin, Continuum modeling of projectile impact and penetration in dry granular media, J. Mech. Phys. Solids 100 (2017) 45–60, http://dx.doi.org/10.1016/j.jmps.2016.12.002.
[13] B. Chandra, R. Hashimoto, S. Matsumi, K. Kamrin, K. Soga, Stabilized mixed material point method for incompressible fluid flow analysis, Comput. Methods Appl. Mech. Engrg. 419 (2024) 116644, http://dx.doi.org/10.1016/j.cma.2023.116644.
[14] B. Chandra, R. Hashimoto, K. Kamrin, K. Soga, Mixed material point method formulation, stabilization, and validation for a unified analysis of free-surface and seepage flow, 2024, arXiv:2402.11719.
[15] X. Zhao, D. Liang, M. Martinelli, MPM simulations of dam-break floods, J. Hydrodyn. 29 (2017) 397–404, http://dx.doi.org/10.1016/S1001-6058(16)60749-7.
[16] S. Kularathna, K. Soga, Implicit formulation of material point method for analysis of incompressible materials, Comput. Methods Appl. Mech. Engrg. 313 (2017) 673–686, http://dx.doi.org/10.1016/j.cma.2016.10.013.
[17] D. Liang, X. Zhao, M. Martinelli, MPM simulations of the interaction between water jet and soil bed, Proceedings of the 1st International Conference on the Material Point Method (MPM 2017), Procedia Eng. vol. 175 (2017) 242–249, http://dx.doi.org/10.1016/j.proeng.2017.01.019.
[18] K. Abe, K. Soga, S. Bandara, Material point method for coupled hydromechanical problems, J. Geotech. Geoenviron. Eng. 140 (2014) 04013033, http://dx.doi.org/10.1061/(ASCE)GT.1943-5606.0001011.
[19] Y. Zhao, J. Choo, Stabilized material point methods for coupled large deformation and fluid flow in porous materials, Comput. Methods Appl. Mech. Engrg. 362 (2020) 112742, http://dx.doi.org/10.1016/j.cma.2019.112742.
[20] S. Kularathna, W. Liang, T. Zhao, B. Chandra, J. Zhao, K. Soga, A semi-implicit material point method based on fractional-step method for saturated soil, Int. J. Numer. Anal. Methods Geomech. 45 (2021) 1405–1436, http://dx.doi.org/10.1002/nag.3207.
[21] S. Bandara, K. Soga, Coupling of soil deformation and pore fluid flow using material point method, Comput. Geotech. 63 (2015) 199–214, http://dx.doi.org/10.1016/j.compgeo.2014.09.009.
[22] K. Soga, E. Alonso, A. Yerro, K. Kumar, S. Bandara, Trends in large-deformation analysis of landslide mass movements with particular emphasis on the material point method, Géotechnique 66 (2016) 248–273, http://dx.doi.org/10.1680/jgeot.15.LM.005.
[23] W. Liang, J. Zhao, H. Wu, K. Soga, Multiscale, multiphysics modeling of saturated granular materials in large deformation, Comput. Methods Appl. Mech. Engrg. 405 (2023) 115871, http://dx.doi.org/10.1016/j.cma.2022.115871.
[24] J. Yu, J. Zhao, W. Liang, S. Zhao, A semi-implicit material point method for coupled thermo-hydro-mechanical simulation of saturated porous media in large deformation, Comput. Methods Appl. Mech. Engrg. 418 (2024) 116462, http://dx.doi.org/10.1016/j.cma.2023.116462.
[25] J. Yu, J. Zhao, W. Liang, S. Zhao, Multiscale modeling of coupled thermo-hydro-mechanical behavior in ice-bonded granular media subject to freeze-thaw cycles, Computers and Geotechnics 171, 106349, http://dx.doi.org/10.1016/j.compgeo.2024.106349.
[26] D. Sulsky, M. Gong, Improving the material-point method, in: K. Weinberg, A. Pandolfi (Eds.), Innovative Numerical Approaches for Multi-Field and Multi-Scale Problems, vol. 81, Springer International Publishing, Cham, 2016, pp. 217–240, http://dx.doi.org/10.1007/978-3-319-39022-2_10.
[27] T.J. O'Hare, P.A. Gourgiotis, W.M. Coombs, C.E. Augarde, An implicit material point method for micropolar solids undergoing large deformations, Comput. Methods Appl. Mech. Engrg. 419 (2024) 116668, http://dx.doi.org/10.1016/j.cma.2023.116668.
[28] M. Cortis, W. Coombs, C. Augarde, M. Brown, A. Brennan, S. Robinson, Imposition of essential boundary conditions in the material point method, Internat. J. Numer. Methods Engrg. 113 (2018) 130–152, http://dx.doi.org/10.1002/nme.5606.
[29] S.G. Bardenhagen, J.U. Brackbill, D. Sulsky, The material-point method for granular materials, Comput. Methods Appl. Mech. Engrg. 187 (2000) 529–541, http://dx.doi.org/10.1016/S0045-7825(99)00338-2.
[30] S.G. Bardenhagen, J.E. Guilkey, K.M. Roessig, J.U. Brackbill, W.M. Witzel, J.C. Foster, An improved contact algorithm for the material point method and application to stress propagation in granular material, CMES Comput. Model. Eng. Sci. 2 (2001) 509–522, http://dx.doi.org/10.3970/cmes.2001.002.509.
[31] J.L. González Acosta, P.J. Vardon, M.A. Hicks, Development of an implicit contact technique for the material point method, Comput. Geotech. 130 (2021) 103859, http://dx.doi.org/10.1016/j.compgeo.2020.103859.
[32] P. Huang, X. Zhang, S. Ma, X. Huang, Contact algorithms for the material point method in impact and penetration simulation, Internat. J. Numer. Methods Engrg. 85 (2011) 498–517, http://dx.doi.org/10.1002/nme.2981.
[33] J.A. Nairn, Modeling imperfect interfaces in the material point method using multimaterial methods, Comput. Model. Eng. Sci. 92 (2013) 271–299.
[34] M.A. Homel, E.B. Herbold, Field-gradient partitioning for fracture and frictional contact in the material point method, Internat. J. Numer. Methods Engrg. 109 (2017) 1013–1044, http://dx.doi.org/10.1002/nme.5317.
[35] M. Xiao, C. Liu, W. Sun, DP-MPM: Domain partitioning material point method for evolving multi-body thermal–mechanical contacts during dynamic fracture and fragmentation, Comput. Methods Appl. Mech. Engrg. 385 (2021) 114063, http://dx.doi.org/10.1016/j.cma.2021.114063.
[36] H. Chen, S. Zhao, J. Zhao, X. Zhou, DEM-enriched contact approach for material point method, Comput. Methods Appl. Mech. Engrg. 404 (2023) 115814, http://dx.doi.org/10.1016/j.cma.2022.115814.
[37] J.A. Nairn, C.C. Hammerquist, G.D. Smith, New material point method contact algorithms for improved accuracy, large-deformation problems, and proper null-space filtering, Comput. Methods Appl. Mech. Engrg. 362 (2020) 112859, http://dx.doi.org/10.1016/j.cma.2020.112859.

[38] M. Steffen, R.M. Kirby, M. Berzins, Analysis and reduction of quadrature errors in the material point method (MPM), Internat. J. Numer. Methods Engrg. 76 (2008) 922–948, http://dx.doi.org/10.1002/nme.2360.
[39] M. Steffen, P.C. Wallstedt, J.E. Guilkey, R.M. Kirby, M. Berzins, Examination and analysis of implementation choices within the material point method (MPM), CMES Comput. Model. Eng. Sci. 31 (2008) 107–128, http://dx.doi.org/10.3970/cmes.2008.031.107.
[40] A. Sadeghirad, R.M. Brannon, J. Burghardt, A convected particle domain interpolation technique to extend applicability of the material point method for problems involving massive deformations, Internat. J. Numer. Methods Engrg. 86 (2011) 1435–1456, http://dx.doi.org/10.1002/nme.3110.
[41] A. Sadeghirad, R.M. Brannon, J.E. Guilkey, Second-order convected particle domain interpolation (CPDI2) with enrichment for weak discontinuities at material interfaces, Internat. J. Numer. Methods Engrg. 95 (2013) 928–952, http://dx.doi.org/10.1002/nme.4526.
[42] J. Guilkey, R. Lander, L. Bonnell, A hybrid penalty and grid based contact method for the material point method, Comput. Methods Appl. Mech. Engrg. 379 (2021) 113739, http://dx.doi.org/10.1016/j.cma.2021.113739.
[43] A. de Vaucorbeil, V.P. Nguyen, Modelling contacts with a total Lagrangian material point method, Comput. Methods Appl. Mech. Engrg. 373 (2021) 113503, http://dx.doi.org/10.1016/j.cma.2020.113503.
[44] C. Liu, W. Sun, ILS-MPM: An implicit level-set-based material point method for frictional particulate contact mechanics of deformable particles, Comput. Methods Appl. Mech. Engrg. 369 (2020) 113168, http://dx.doi.org/10.1016/j.cma.2020.113168.
[45] Y. Jiang, M. Li, C. Jiang, F. Alonso-Marroquin, A hybrid material-point spheropolygon-element method for solid and granular material interaction, Internat. J. Numer. Methods Engrg. 121 (2020) 3021–3047, http://dx.doi.org/10.1002/nme.6345.
[46] X. Li, Y. Fang, M. Li, C. Jiang, BFEMP: Interpenetration-free MPM–FEM coupling with barrier contact, Comput. Methods Appl. Mech. Engrg. 390 (2022) 114350, http://dx.doi.org/10.1016/j.cma.2021.114350.
[47] M.A. Puso, T.A. Laursen, A mortar segment-to-segment contact method for large deformation solid mechanics, Comput. Methods Appl. Mech. Engrg. 193 (2004) 601–629, http://dx.doi.org/10.1016/j.cma.2003.10.010.
[48] A. Popp, M.W. Gee, W.A. Wall, A finite deformation mortar contact formulation using a primal–dual active set strategy, Internat. J. Numer. Methods Engrg. 79 (2009) 1354–1391, http://dx.doi.org/10.1002/nme.2614.
[49] H. Fang, Z.-Y. Yin, M. Peng, D. Zhang, Improved SNS-PFEM framework with dual mortar method to model geotechnical large deformation contact problems, Comput. Methods Appl. Mech. Engrg. 412 (2023) 116091, http://dx.doi.org/10.1016/j.cma.2023.116091.
[50] M. Zhou, Q. Fang, C. Peng, A mortar segment-to-segment contact method for stabilized total-Lagrangian smoothed particle hydrodynamics, Appl. Math. Model. 107 (2022) 20–38, http://dx.doi.org/10.1016/j.apm.2022.02.022.
[51] H. Fang, Z.-Y. Yin, D. Zhang, L. Cao, A hydro-mechanical coupled contact method for two-phase geotechnical large deformation problems within the SNS-PFEM framework, Comput. Methods Appl. Mech. Engrg. 420 (2024) 116743, http://dx.doi.org/10.1016/j.cma.2023.116743.
[52] Y. Jiang, Y. Zhao, C.E. Choi, J. Choo, Hybrid continuum–discrete simulation of granular impact dynamics, Acta Geotech. (2022) http://dx.doi.org/10.1007/s11440-022-01598-2.
[53] Y. Zhao, J. Choo, Y. Jiang, L. Li, Coupled material point and level set methods for simulating soils interacting with rigid objects with complex geometry, Comput. Geotech. 163 (2023) 105708, http://dx.doi.org/10.1016/j.compgeo.2023.105708.
[54] Y. Zhao, M. Li, C. Jiang, J. Choo, Mapped material point method for large deformation problems with sharp gradients and its application to soil-structure interactions, Int. J. Numer. Anal. Methods Geomech. 48 (2024) 2334–2355, http://dx.doi.org/10.1002/nag.3731.
[55] C. Jiang, C. Schroeder, A. Selle, J. Teran, A. Stomakhin, The affine particle-in-cell method, ACM Trans. Graph. 34 (2015) 51:1–51:10, http://dx.doi.org/10.1145/2766996.
[56] C. Jiang, C. Schroeder, J. Teran, An angular momentum conserving affine-particle-in-cell method, J. Comput. Phys. 338 (2017) 137–164, http://dx.doi.org/10.1016/j.jcp.2017.02.050.
[57] S.G. Bardenhagen, E.M. Kober, The generalized interpolation material point method, Comput. Model. Eng. Sci. 5 (2004) 477–496.
[58] K. Nakamura, S. Matsumura, T. Mizutani, Taylor particle-in-cell transfer and kernel correction for material point method, Comput. Methods Appl. Mech. Engrg. 403 (2023) 115720, http://dx.doi.org/10.1016/j.cma.2022.115720.
[59] B. Holmedal, Spin and vorticity with vanishing rigid-body rotation during shear in continuum mechanics, J. Mech. Phys. Solids 137 (2020) 103835, http://dx.doi.org/10.1016/j.jmps.2019.103835.
[60] T.J. Charlton, W.M. Coombs, C.E. Augarde, iGIMP: An implicit generalised interpolation material point method for large deformations, Comput. Struct. 190 (2017) 108–125, http://dx.doi.org/10.1016/j.compstruc.2017.05.004.
[61] F.H. Harlow, The particle-in-cell computing method for fluid dynamics, Methods Comput. Phys. 3 (1964) 319–343.
[62] J.U. Brackbill, H.M. Ruppel, FLIP: A method for adaptively zoned, particle-in-cell calculations of fluid flows in two dimensions, J. Comput. Phys. 65 (1986) 314–343, http://dx.doi.org/10.1016/0021-9991(86)90211-1.
[63] C.C. Hammerquist, J.A. Nairn, A new method for material point method particle updates that reduces noise and enhances stability, Comput. Methods Appl. Mech. Engrg. 318 (2017) 724–738, http://dx.doi.org/10.1016/j.cma.2017.01.035.
[64] K.-Y. He, W. Liang, Z.-Y. Yin, Y.-F. Jin, An efficient material point method framework based on the affine matrix, Comput. Geotech. 163 (2023) 105712, http://dx.doi.org/10.1016/j.compgeo.2023.105712.
[65] H. Fang, Z.-Y. Yin, D. Zhang, Q. Fang, Unified framework for geotechnical cross-contact problems with interfacial fluid flow, Int. J. Mech. Sci. 269 (2024) 109047, http://dx.doi.org/10.1016/j.ijmecsci.2024.109047.
[66] A. Popp, Mortar Methods for Computational Contact Mechanics and General Interface Problems (Ph.D. thesis), Technische Universität München, 2012.
[67] Y. Zhao, J. Choo, Y. Jiang, M. Li, C. Jiang, K. Soga, A barrier method for frictional contact on embedded interfaces, Comput. Methods Appl. Mech. Engrg. 393 (2022) 114820, http://dx.doi.org/10.1016/j.cma.2022.114820.
[68] M. Li, Z. Ferguson, T. Schneider, T. Langlois, D. Zorin, D. Panozzo, C. Jiang, D.M. Kaufman, Incremental potential contact: Intersection-and inversion-free, large-deformation dynamics, ACM Trans. Graph. 39 (2020) 49:49:1–49:49:20, http://dx.doi.org/10.1145/3386569.3392425.
[69] V. Smilauer, E. Catalano, B. Chareyre, S. Dorofeenko, J. Duriez, N. Dyck, J. Elias, B. Er, A. Eulitz, A. Gladky, N. Guo, C. Jakob, F. Kneib, J. Kozicki, D. Marzougui, R. Maurin, C. Modenese, L. Scholtes, L. Sibille, J. Stransky, T. Sweijen, K. Thoeni, C. Yuan, Yade Documentation, second ed., Zenodo, 2015, http://dx.doi.org/10.5281/zenodo.34073.
[70] H. Wu, W. Wu, W. Liang, F. Dai, H. Liu, Y. Xiao, 3D DEM modeling of biocemented sand with fines as cementing agents, Int. J. Numer. Anal. Methods Geomech. 47 (2023) 212–240, http://dx.doi.org/10.1002/nag.3466.
[71] P. Wang, Z.-Y. Yin, P.-Y. Hicher, Y.-J. Cui, Micro-mechanical analysis of one-dimensional compression of clay with DEM, Int. J. Numer. Anal. Methods Geomech. 47 (2023) 2706–2724, http://dx.doi.org/10.1002/nag.3597.
[72] E. Wyser, Y. Alkhimenkov, M. Jaboyedoff, Y.Y. Podladchikov, A fast and efficient MATLAB-based MPM solver: fMPMM-solver v1.1, Geosci. Model Dev. 13 (2020) 6265–6284, http://dx.doi.org/10.5194/gmd-13-6265-2020.
[73] K.L. Johnson, Contact Mechanics, Cambridge University Press, 1987.
[74] J.P. Gray, J.J. Monaghan, R.P. Swift, SPH elastic dynamics, Comput. Methods Appl. Mech. Engrg. 190 (2001) 6641–6662, http://dx.doi.org/10.1016/S0045-7825(01)00254-7.
[75] J.J. Monaghan, SPH without a tensile instability, J. Comput. Phys. 159 (2000) 290–311, http://dx.doi.org/10.1006/jcph.2000.6439.
[76] V.P. Nguyen, A. de Vaucorbeil, C. Nguyen-Thanh, T.K. Mandal, A generalized particle in cell method for explicit solid dynamics, Comput. Methods Appl. Mech. Engrg. 371 (2020) 113308, http://dx.doi.org/10.1016/j.cma.2020.113308.

[77] W. Liang, K.-Y. He, Y.-F. Jin, Z.-Y. Yin, A gradient-smoothed material point method for reducing cell crossing noise in large deformation problems, Comput. Geotech. 169 (2024) 106169, http://dx.doi.org/10.1016/j.compgeo.2024.106169.

[78] A.P.C. Dias, S.P.B. Proenca, M.L. Bittencourt, High-order mortar-based contact element using NURBS for the mapping of contact curved surfaces, Comput. Mech. 64 (2019) 85–112, http://dx.doi.org/10.1007/s00466-018-1658-6.

[79] G. Mollon, Mixtures of hard and soft grains: Micromechanical behavior at large strains, Granul. Matter 20 (2018) 39, http://dx.doi.org/10.1007/s10035-018-0812-3.

[80] Q. Ku, J. Zhao, G. Mollon, S. Zhao, Compaction of highly deformable cohesive granular powders, Powder Technol. 421 (2023) 118455, http://dx.doi.org/10.1016/j.powtec.2023.118455.

[81] A. de Vaucorbeil, V.P. Nguyen, C.R. Hutchinson, A total-Lagrangian material point method for solid mechanics problems involving large deformations, Comput. Methods Appl. Mech. Engrg. 360 (2020) 112783, http://dx.doi.org/10.1016/j.cma.2019.112783.